Volatile-rich Metasomatism in the Cratonic Mantle beneath SW Greenland: Link to Kimberlites and Mid-lithospheric Discontinuities

Sonja Aulbach[1]*, Jing Sun[1,2], Sebastian Tappe[3], Heidi E. Höfer[1] and Axel Gerdes[1]

[1]Goethe Universität, Institut für Geowissenschaften, Altenhöferallee 1, 60438 Frankfurt, Germany; [2]State Key Laboratory of Lithospheric Evolution, Institute of Geology and Geophysics, Chinese Academy of Sciences, Beijing 100029, China; [3]Department of Geology, University of Johannesburg, PO Box 524, 2006 Auckland Park, South Africa

*Corresponding author. Telephone: +49-069-798-40125. E-mail: s.aulbach@em.uni-frankfurt.de

ABSTRACT

The cratonic part of Greenland has been a hotspot of scientific investigation since the discovery of some of the oldest crust on Earth and of significant diamond potential in the underlying lithospheric mantle, the characterization of which remains, however, incomplete. We applied a detailed petrographic and *in situ* analytical approach to a new suite of fresh kimberlite-borne peridotite xenoliths, recovered from the North Atlantic craton in SW Greenland, to unravel the timing and nature of mantle metasomatism, and its link to the formation of low-volume melts (e.g. kimberlites) and to geophysically detectible discontinuities. Two types of mineralogies and metasomatic styles, occurring at two depth intervals, are recognized. The first type comprises lherzolites, harzburgites and dunites, some phlogopite-bearing, which occur from ~100–170 km depth. They form continuous trends towards lower mineral Mg# at increasing TiO_2, MnO and Na_2O and decreasing NiO contents. These systematics are ascribed to metasomatism by a hydrous silicate melt precursor to c. 150 Ma kimberlites, in the course of rifting, decompression and lithosphere thinning. This metasomatism was accompanied by progressive garnet breakdown, texturally evident by pyroxene–spinel assemblages occupying former coarse grains and compositionally evident by increasing concentrations of elements that are compatible in garnet (Y, Sc, In, heavy rare earth elements) in newly formed clinopyroxene. Concomitant sulphide saturation is indicated by depletion in Cu, Ni and Co. The residual, more silica-undersaturated and potentially more oxidizing melts percolated upwards and metasomatized the shallower lithospheric mantle, which is composed of phlogopite-bearing, texturally equilibrated peridotites, including wehrlites, showing evidence for recent pyroxene-breakdown. This is the second type of lithology, which occurs at ~90–110 km depth and is inferred to have highly depleted protoliths. This type is compositionally distinct from lherzolites, with olivine having higher Ca/Al, but lower Al and V contents. Whereas low Al may in part reflect lower equilibration temperatures, low V is ascribed to a combination of intrinsically more oxidizing mantle at lower pressure and oxidative metasomatism. The intense metasomatism in the shallow cratonic mantle lithosphere contrasts with the strong depletion recorded in the northwestern part of the craton, which at 590–550 Ma extended to >210 km depth, and suggests loss of ~40 km of lithospheric mantle, also recorded in the progressive shallowing of magma sources during the breakup of the North Atlantic craton. The concentration of phlogopite-rich lithologies in a narrow depth interval (~90–110 km) overlaps with a negative seismic velocity gradient that is interpreted as a mid-lithospheric discontinuity beneath western Greenland. This is suggested to be a manifestation of small-volume volatile-rich magmatism, which paved the way for Mesozoic kimberlite, ultramafic lamprophyre, and carbonatite emplacement across the North Atlantic craton.

INTRODUCTION

Earth's cratons are ancient continental cores that archive information on the earliest crust and mantle dynamics, which were significantly different from those of the present day (e.g. Arndt & Nisbet, 2012; Aulbach, 2012; Santosh, 2013). Understanding the causes of cratonic durability and identification of processes leading to their destruction is therefore of considerable scientific interest. Cratons owe their longevity to their uniquely melt-depleted lithospheric mantle keels, which provide chemical buoyancy, and high viscosity that renders them resistant to entrainment into the convecting mantle and protects them from later accretion processes at the craton margins (Griffin *et al.*, 2009; Wang *et al.*, 2014). Mantle sections from the Kaapvaal craton (southern Africa), the Slave craton (Canada), and the Siberian craton have been particularly well studied, and they provide benchmark models for our understanding of cratonic lithosphere origin and evolution.

A variety of geochemical tools have been applied to mantle peridotites to decipher the origin and evolution of cratons. Because in mantle peridotites incompatible trace elements partition predominantly into garnet (when present) and clinopyroxene (cpx) (e.g. Witt-Eickschen & O'Neill, 2005; Adam & Green, 2006), including those that are used for age dating and fingerprinting of mantle sources (Rb–Sr, Sm–Nd, Lu–Hf), these minerals have traditionally been the focus of detailed trace element and isotopic investigations [reviewed by Pearson *et al.* (2003)]. By contrast, olivine was until recently mainly characterized for its major and minor element composition, in particular using electron microprobe and secondary ion mass spectrometry (SIMS), as well as some early work using laser ablation inductively coupled plasma mass spectrometry (LA-ICP-MS) systems (e.g. O'Reilly *et al.*, 1997; Eggins *et al.*, 1998; Glaser *et al.*, 1999; Sobolev *et al.*, 2007, 2009; Rehfeldt *et al.*, 2008). With the advent of ever more sensitive instrumentation and laser ablation devices that afford *in situ* measurements at very low detection limits, with high spatial resolution and limited inter-element fractionation, olivine has been 'rediscovered' as an archive of petrogenetic information on the origin and evolution of mantle lithosphere (De Hoog *et al.*, 2010; Foley *et al.*, 2013; Smith, 2013). Elements that more strongly partition into garnet have shown promise in distinguishing between spinel- and garnet-bearing mantle (e.g. Mn and Sc), whereas strongly incompatible elements have large concentration ranges in olivine that co-vary with bulk-rock concentrations and are useful as petrogenetic indicators of partial melting and re-enrichment (e.g. Ti and Y) (De Hoog *et al.*, 2010). In addition, Ti–Ca relationships have been suggested to fingerprint silicate melts versus carbonate–silicate melts as the enriching agents (Foley *et al.*, 2013), and increased Li content was proposed to indicate interaction with fluids (e.g. in subduction zones; Smith, 2013), and continental crustal input (Foley *et al.*, 2013; Prelevic *et al.*, 2013). The partitioning of some minor and trace elements in olivine has further been known for some time to be temperature ± pressure dependent (Witt-Eickschen & O'Neill, 2005). Recently, Al-, Cr- and V-based thermometers were experimentally or empirically calibrated for garnet peridotites, which have little pressure dependence and rather successfully reproduce known temperatures, even for spinel peridotites (De Hoog *et al.*, 2010; Smith, 2013; Bussweiler *et al.*, 2017). The analytical development has gone hand in hand with the acquisition of more complete sets of trace element partition coefficients between olivine and coexisting minerals or melts in nature and experiment (Witt-Eickschen & O'Neill, 2005; Adam & Green, 2006).

Here, we present petrographic and *in situ* major and trace element data for a suite of exceptionally fresh mantle-derived peridotite xenoliths from the Mesozoic Pyramidefjeld and Midternaes kimberlite sheets in cratonic SW Greenland, which were emplaced *c.* 150 myr ago (Andrews & Emeleus, 1975; Emeleus & Andrews, 1975; Frei *et al.*, 2008; Larsen *et al.*, 2009). Major and trace elements, complemented by Sr–Nd isotope data, are used to identify samples that have been modified by interaction with melts (metasomatism) during their long-term residence in the mantle lithosphere and to obtain information on enrichment processes following initial melt depletion. Given that olivine is dominant in these samples, it is imperative that the geochemical signatures contained in this mineral be exploited to obtain information on the origin and evolution of the lithospheric mantle beneath cratonic Greenland. Taken together, the data allow us to discuss links between strong modal and cryptic enrichment of the shallow lithosphere to constrain (1) the timing and nature of small-volume alkaline ultramafic melts that percolated the mantle prior to kimberlite magmatism, (2) the generation of seismically slow mantle regions at mid-lithospheric levels, (3) textural evidence for garnet destabilization in the context of extensive Mesozoic rifting (Tappe *et al.*, 2007), and (4) redox effects accompanying metasomatism as gauged by V–Sc relationships in constituent minerals.

GEOLOGY, SAMPLES AND PRIOR WORK

The cratonic part of Greenland, a constituent of the North Atlantic craton (hereafter referred to as GNAC), contains some of the oldest rocks on Earth, such as the Eoarchaean (3·8–3·7 Ga) Isua Supracrustal Belt, including evidence for the earliest (Hadaean) mantle source

identified so far (Bennett *et al.*, 2007). The GNAC consists predominantly of several tonalite–trondhjemite–granodiorite (TTG) terranes that formed mostly between 3·0 and 2·8 Ga, but include up to 3·7 Ga gneisses as well as cross-cutting 3·0–2·6 Ga granite sheets, overlain by fragmented, mafic supracrustal belts (Rosing *et al.*, 2001; Nutman *et al.*, 2004; Nutman & Friend, 2009). The lithospheric mantle beneath this region has attracted considerable attention not least because of its diamond potential and exceptional degree of depletion (Bernstein *et al.*, 1998, 2006; Bizzarro & Stevenson, 2003; Hutchison *et al.*, 2007; Hutchison & Heaman, 2008; Sand *et al.*, 2009; Tappe *et al.*, 2011*b*). The GNAC was assembled during a period of Neoarchaean collisional tectonics (Griffin *et al.*, 2004; Pearson & Wittig, 2008; Windley & Garde, 2009; Tappe *et al.*, 2011*b*), and the craton and its surrounding Paleoproterozoic mobile belts were intruded by deep-rooted kimberlite, ultramafic lamprophyre and alkali basalt magmas that brought mantle-derived fragments (mantle xenoliths) to the surface (Bernstein *et al.*, 1998, 2006, 2013; Bizzarro & Stevenson, 2003; Wittig *et al.*, 2008, 2010; Sand *et al.*, 2009; Tappe *et al.*, 2011*b*).

The GNAC is bordered in the north and south by younger gneisses that were metamorphosed during the Nagssugtoqidian and Ketilidian orogenies 1·7–1·9 Gyr ago, which relate to Laurentian plate assembly (Hoffman, 1989). Several failed rifting episodes at 2·0 Ga, 1·4–1·2 Ga and 0·61–0·55 Ga led to the emplacement of mafic dyke swarms and of volumetrically minor ultramafic alkaline magmas. This lithospheric stretching affected the underlying continental lithospheric mantle, leading to its partial destruction and replacement with asthenospheric mantle (Tappe *et al.*, 2007, 2012). At 140–100 Ma, the development of rift basins and emplacement of alkaline basalts signalled the beginning of the opening of the North Atlantic Ocean, with breakup of the NAC along the Labrador Sea margins at 60–30 Ma (Tappe *et al.*, 2007, 2009; Larsen *et al.*, 2009).

Forty-two peridotite xenoliths were collected from the Mesozoic Pyramidefjeld and Midternaes kimberlite dyke localities in SW Greenland, at the southwestern margin of the GNAC in 2007 (Fig. 1). The kimberlite magmas intruded *c*. 150 myr ago (Emeleus & Andrews, 1975; Frei *et al.*, 2008; Larsen *et al.*, 2009), with Midternaes being somewhat closer to the GNAC centre and yielding xenoliths with slightly higher equilibration temperatures and pressures relative to Pyramidefjeld, possibly reflecting a deeper cratonic root (Hutchison *et al.*, 2007). Out of the 42 xenoliths, the 37 freshest mantle xenoliths were chosen for the present study. The xenoliths are up to ∼20 cm in size and range from garnet-free dunites and harzburgites to clinopyroxene- and phlogopite-bearing peridotites, including wehrlites (Table 1).

Prior studies have shown that the shallow mantle beneath parts of Greenland (Wiedemann Fjord, central craton, and southern and northern margins of the western GNAC) is unusually depleted in magmaphile
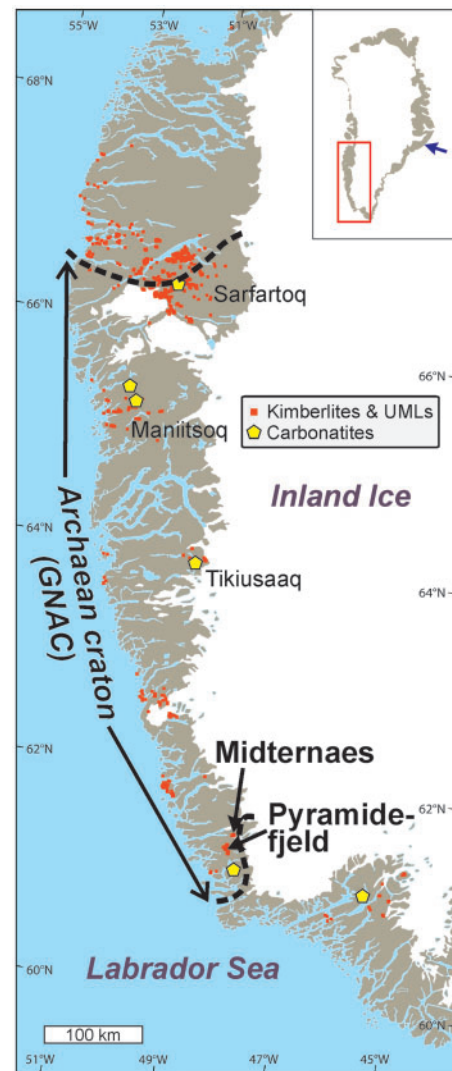

Fig. 1. Map of cratonic SW Greenland, which forms part of the North Atlantic craton (NAC), indicating the Pyramidefjeld and Midternaes kimberlite localities. Locations of the Sarfartoq, Maniitsoq, and Tikiusaaq kimberlite fields are also shown. Boundaries of the GNAC (Greenland North Atlantic craton) with Palaeoproterozoic mobile belts in the north and south are indicated with thick dashed contour lines [modified from Tappe *et al.* (2009)]. Inset shows an outline of Greenland with the Wiedemann Fjord xenolith locality (arrow) in the eastern part of the craton. UML, ultramafic lamprophyre.

elements owing to loss of partial melt, which is evident in high forsterite contents in olivine, low modes of primary clinopyroxene, and low contents of incompatible elements such as Al_2O_3, CaO, Pd and Pt (Bernstein *et al.*, 1998, 2006; Wittig *et al.*, 2010). Unusually olivine-rich spinel harzburgites from southeastern Greenland (Fig. 1, inset) last equilibrated at 850°C and 1 GPa and have experienced polybaric extraction of about 40% broadly komatiitic partial melt in the Archaean, based on depleted $^{187}Os/^{188}Os$ (Bernstein *et al.*, 1998; Hanghøj *et al.*, 2001). In contrast, lherzolites with up to 25 vol. % orthopyroxene (opx) are much less depleted and have more radiogenic Os, consistent with metasomatic refertilization (Hanghøj *et al.*, 2001). Mantle xenoliths from

Table 1: Petrographical details and pressure–temperature estimates for peridotites from SW Greenland

Sample	Assemblage	Rock type	Microstructure
476407a	ol opx phl	phl harz	Coarse-porphyroclastic, foliated
476407c1	ol ?alt/cpx phl	phl perid	Coarse-granoblastic, mildly foliated
476407c2	ol ?alt/cpx phl	phl perid	Coarse-porphyroclastic, mildly foliated
476407d	ol phl sp	phl dun	Coarse-granoblastic
476407i	ol (cpx phl)	phl wehr	Coarse-granoblastic, foliated
476407j	ol	mega-crystalline dun	
476414d	ol cpx	wehr	Coarse-granoblastic
476415a	ol opx cpx (phl)	phl lherz	Coarse-grained granular
476415b	ol opx cpx sp	lherz	Coarse-grained granoblastic
476415b2a	ol opx cpx sp	lherz	Medium-grained granoblastic
476415b2b	ol	dun	Coarse-porphyroclastic, mildly foliated
476415b2n	ol opx (cpx)	lherz	Medium-granoblastic
476415b2o	ol opx cpx phl	phl lherz	Coarse-granoblastic, mildly foliated
476415c	ol cpx phl	phl wehr	Medium-granoblastic
476415d	ol cpx phl	phl wehr	Medium-porphyroclastic, mildly foliated
476415e	ol opx cpx1 sp	lherz	Coarse-granoblastic
476415e	ol opx cpx2 sp		
476415f1	ol cpx phl sp	phl wehr	Medium-porphyroclastic, mildly foliated
476415f2	ol cpx phl	phl wehr	Medium-porphyroclastic, mildly foliated
476415g	ol opx cpx	lherz	Coarse-granoblastic
476415h1	ol opx cpx	lherz	Coarse-granoblastic, mildly foliated
476415h2	ol opx cpx	lherz	Coarse-grained porphyroclastic
476415i	ol sp	dun	Coarse-porphyroclastic, mildly foliated
476415j	ol cpx (phl)	phl wehr	Coarse-grained porphyroclastic
476415o	ol opx cpx	phl lherz	Coarse-granular
476415p	ol cpx phl	phl wehr	Medium-granoblastic, mildly foliated
476415q	ol ?alt/cpx phl (sp)	phl perid	Coarse-porphyroclastic
476415r	ol opx cpx phl	phl lherz	Medium-porphyroclastic, foliated
476424b1	ol opx cpx	lherz	Coarse-grained porphyroclastic
476424b2	ol (cpx phl)	phl wehr	Medium-grained granoblastic
476424m	ol (cpx phl)	phl wehr	Medium-granular, foliated
476424n	ol (opx cpx)	lherz	Coarse-granoblastic
476424o	ol	dun	Medium-porphyroblastic, tabular
476424q	ol opx cpx phl	phl lherz	Coarse-porphyroclastic
476424s	ol cpx (phl sp)	phl wehr	Coarse porphyroclastic, mildly foliated
476424t	ol ?alt/cpx (sp)	perid	Medium-granoblastic
476424u	ol ?alt/cpx (sp)	perid	Medium-grained porphyroclastic

590–550 Ma kimberlites and ultramafic lamprophyres in the Sarfartoq–Maniitsoq areas of the GNAC (Fig. 1) have been shown to lie on a pressure–temperature array consistent with a layered lithospheric mantle extending to ~215 km depth; that is, well into the diamond stability field (Bizzarro & Stevenson, 2003; Sand *et al.*, 2009). The shallow, highly depleted lithospheric mantle layer has been constrained to lie between ~90 to 115 km depth and to be underlain by a less depleted, compositionally heterogeneous layer consisting of lherzolite and wehrlite in addition to harzburgite (Sand *et al.*, 2009). Lithosphere formation in that area was dated to the Meso- and Neoarchaean, based on Re–Os and Pb–Pb isotope constraints, both of which also revealed Proterozoic metasomatic episodes (Hanghøj *et al.*, 2001; Wittig *et al.*, 2010; Tappe *et al.*, 2011*b*; van Acken *et al.*, 2017).

SAMPLE PREPARATION, ANALYTICAL TECHNIQUES AND DATA REDUCTION

Xenoliths were cut out of the kimberlite and thick sections (100 μm) were prepared from blocks. Following petrographic investigation with a polarizing microscope,

major and trace element concentrations were determined *in situ* by electron probe microanalysis (EPMA) and by laser ablation inductively coupled plasma mass spectrometry (LA-ICP-MS) to extract spatially resolved information. Multiple spots per grain and multiple grains per sample ($n = 5$ where possible) were analysed to test intra-grain and inter-grain compositional homogeneity. All work was carried out in the Mineralogy Unit of the Institute of Geosciences at Goethe-Universität Frankfurt.

Electron microprobe analyses
Major element analyses were obtained for all silicate minerals and spinel with a JEOL Superprobe JXA-8900 electron microprobe, at 15 kV accelerating voltage, a beam current of 20 nA and a nominal beam diameter of 1 μm. Natural and synthetic standards were measured as unknowns to check accuracy.

Laser ablation inductively coupled plasma mass spectrometry (LA-ICP-MS)
For trace element analyses, a Thermo Finnigan Element2 ICP-MS system was linked to an M-50 HR laser system (Resonetics), which employs a low-wavelength laser

Table 1: Continued

Sample	T(TA98) cpx–opx	T(NG10) Ca-in-opx	ΔT	T(Al-ol) ol	T[Al-ol @42 mW m^2]	P[42 mW m^2] @Al-ol]
476407a	*P* = 4 GPa	981		999	Iterative solutions	1016	43
476407c1				872		842	33
476407c2				Al b.d.l.		Al b.d.l.	Al b.d.l.
476407d				973		977	41
476407i				898		874	35
476407j				684		635	27
476414d				961		959	40
476415a	907	932	−25	991		1004	42
476415b	960	907	53	1008		1029	44
476415b2a	1251	922	*329*	975		980	41
476415b2b				804		761	30
476415b2n		886		937		926	38
476415b2o	922	927	−5	989		1001	42
476415c				830		791	31
476415d				884		857	34
476415e	911	927	−15	1042		1086	48
476415e	1223	927	*296*	1042		1086	48
476415f1				798		756	30
476415f2				795		753	30
476415g	940	943	−3	973		976	41
476415h1	964	954	10	1016		1042	45
476415h2	944	973	−29	1000		1017	43
476415i				899		876	35
476415j				774		729	29
476415o	972	973	−2	988		998	42
476415p				691		642	27
476415q				710		661	27
476415r	950	1027	−77	996		1011	43
476424b1	1039	1079	−40	1087		1170	55
476424b2				762		716	29
476424m				779		735	29
476424n				1085		1165	55
476424o				743		696	28
476424q	878	875	3	823		785	31
476424s				847		813	32
476424t				747		700	28
476424u				751		705	28

ol, olivine; opx, orthopyroxene; phl, phlogopite; cpx, clinopyroxene; sp, spinel; alt, altered; hz, harzburgite; dun, dunite; wehr, wehrlite; lherz, lherzolite; perid, peridotite; b.d.l., below detection limit. Minerals in parentheses were too small or too altered to be analysed; phlogopite associated with late kimberlite infiltration is not considered. TA98, Taylor (1998); NG, Nimis & Grütter (2010); Al-ol, De Hoog *et al.* (2010); Al-ol@42 mW m^{-2}, iterative solution with the garnet peridotite-derived geothermal gradient corresponding to a surface heat flow of 42 mW m^{-2} from Nielsen *et al.* (2008). Values in italics highlight highly discrepant results for T[TA98] and T[NG10].

(193 nm) with increased sensitivity and more stable signals compared with higher wavelength types. It is equipped with a dual-volume sample cell that keeps the sample volume small and constant. Using the standard reference material NIST 612 (a glass matrix doped with 61 elements at a nominal concentration of 50 ppm) as a calibration standard, natural basalt glass reference material BIR-1G as a secondary standard to monitor performance and Si, as determined by EPMA, for internal standardization, a laser ablation routine was established that would return accurate and precise trace element concentrations for peridotite minerals.

Olivine and opx are noted for having very low concentrations of many large-ion lithophile and high field strength elements (e.g. Foley *et al.*, 2013). Because these minerals have matrices that differ significantly from the glass standard, which has consequences for the type and amount of molecular interferences that can form, different routines involving medium- and low-resolution analyses were tested using mineral separates from a San Carlos peridotite xenolith. San Carlos is known for its compositionally homogeneous minerals, which are frequently used as certified or in-house microbeam standards for elemental analysis (e.g. Seitz *et al.*, 1999). To improve detection limits, and given that olivine and opx in the sample suite have large grain sizes (millimetres to centimetres), a large laser spot diameter of 80 μm and a laser pulse frequency of 12 Hz with an energy of 100 mJ were used, whereas a 30 μm spot size was used in the analysis of relatively small cpx and phlogopite crystals.

Trace element data reduction and quality assurance

The LA-ICP-MS raw data were reduced using the GLITTER software (Griffin *et al.*, 2008), where limits of

detection (LOD; 3σ above background) are calculated assuming a Gaussian distribution, which can yield very low LOD when very few counts are detected in the background. We therefore also provide limits of quantification (LOQ; 10σ above background) as a measure of the lowest concentrations that can be reliably quantified. A comparison of recommended values for BIR-1 with those obtained here shows agreement within 15% for most elements, exceptions being Li, Zn, Mo and Pb (+20–30%) and Ta (+70%). A large number of trace elements were measured in both low- and medium-resolution mode. The tests showed that for San Carlos olivine, Ca, Sc and Ga were systematically significantly higher when measured in low-resolution mode, whereas for V, Cr, Mn, Co, Ni and Zn deviations were on average ≤+7%, and Cu was on average lower by 30%. Results for Cu are therefore given for low-resolution analyses. In keeping with Aulbach & Viljoen (2015), we used Ba, which is strongly enriched in kimberlite compared with olivine and pyroxenes (Table 2), to identify any host magma contamination. Additional detailed information on data reduction and quality control is given in Supplementary Data Electronic Appendix 1; supplementary data are available for downloading at http://www.petrology.oxfordjournals.org. The full dataset is given in the Supplementary Data Appendices, whereas Table 2 reflects only contamination-free data, which are described below and used in the calculation of apparent distribution coefficients and plotted in the figures.

Isotope dilution ICP-MS

Despite their general freshness, clean cpx separates for isotope analyses could be obtained for only four samples, owing to the small grain size and low modal abundances. The separates were leached for 30 min in 6M HCl and rinsed three times in MQ H_2O prior to dissolution in a mixture of twice-distilled HF and HNO_3. Radiogenic isotope data were acquired in Frankfurt following established sample preparation and analytical routines (Lazarov *et al.*, 2009; Luchs *et al.*, 2013). After addition of a mixed Sm–Nd spike, cpx separates were digested and purified using a three-step column chromatographic approach. This was followed by measurement of Sr–Sm–Nd isotope ratios by multi-collector ICP-MS (Thermo-Finnigan Neptune) using a glass spray chamber. Full procedural blanks are 0·4 ppb Sr, 0·01 ppb Sm and 0·02 ppb Nd. No blank correction was applied. The pure Sr standard solution NBS987 and ∼50 mg of the basaltic reference material BIR-1 gave $^{87}Sr/^{86}Sr$ of 0·710223 ± 0·000038 (2σ, $n = 8$) and of 0·703175 ± 0·000080 (2σ, $n = 2$), respectively (GeoReM preferred values for BIR-1 are 0·703108–0·70313; Jochum *et al.*, 2005). A 25 ppb Nd standard solution (Merck) gave $^{143}Nd/^{144}Nd$ of 0·511692 (±0·000023; $n = 3$) and BIR-1 gave 0·513086 ± 0·000018 ($n = 2$) (GeoReM preferred values are 0·51305–0·51313).

RESULTS

Petrography

Plane-polarized light images are shown in Figs 2 and 3. Based on the primary mineral assemblage identified in thick section (i.e. not considering texturally unequilibrated, late-added phlogopite), the samples are classified as lherzolites (olivine, opx, cpx ± spinel), harzburgites (olivine, opx ± spinel), dunites (olivine ± spinel) and wehrlites (olivine, cpx ± spinel), and phlogopite-bearing varieties thereof (described hereafter with the prefix 'phl-'). Where the former existence of pyroxenes, now present as cryptocrystalline pseudomorphs with well-defined grain boundaries (Fig. 3e), is suspected, which is the case for five samples, they are grouped as peridotites or phl-peridotites. Wehrlites contain seemingly texturally equilibrated (indicated by 120° grain boundaries), but irregularly distributed cpx and phlogopite (Fig. 2d). Many samples are highly fractured and partially altered, especially where veins—presumably filled with kimberlite material—pervade the sample. Most are medium- to coarse-porphyroclastic rocks with weak foliation defined by shape-preferred orientation of olivine.

Olivine is the dominant phase in all samples, sometimes defining a foliation. Multiple sizes and shapes can be present (e.g. 476415d; Fig. 3a), including larger porphyroclasts (3–7 mm) with bent extinction lamellae that have an anhedral shape or undulose extinction, euhedral medium-sized grains (0·5–0·8 mm) extinguishing homogeneously and small euhedral equant grains (0·1–0·2 mm) occurring at the boundaries of large olivine grains, pointing to post-deformation growth.

When present, opx is a subordinate phase with euhedral to subhedral shape, sometimes showing lobate grain boundaries with cpx or olivine (e.g. 476415a; Fig. 3b). Porphyroclasts up to 5 mm are occasionally observed (e.g. 476415o). It may be distributed heterogeneously, occurring in strings of grains (e.g. 476407a; Fig. 3c). Exsolution of cpx ± ?spinel is observed in some grain cores (Fig. 2a, inset).

Clinopyroxene grains are generally smaller than olivine (∼1–3 mm) and frequently anhedral, but also occur as subhedral, smaller grains and as rims on opx and olivine (e.g. 476424q; Fig. 3d). They show a strong green colour and occur either as discrete grains or in clusters, or are intergrown with phlogopite (Fig. 2c). In some samples, a microcrystalline green mass fills out well-defined subhedral grain shapes interpreted as former pyroxene (e.g. 476424u; Fig. 3e).

Phlogopite is a frequent minor phase and generally appears to be in textural equilibrium with the other minerals. Grains are subhedral to anhedral and may be intergrown with spinel or cpx (Fig. 2c). They sometimes show shape-preferred orientation, indicative of deformation during or subsequent to their precipitation. Occasionally, large clusters of phlogopite are present (e.g. 476407a; Fig. 3c). In some samples, phlogopite occurs as a texturally late, anhedral phase associated

Table 2: Median major element (wt %) and trace element (ppm) compositions for silicate minerals in various xenolith types from the SW craton margin of Greenland

Rock type:		ph-lh	lh	ph-wehr	dun	perid		ph-lh	lh
			Olivine				Orthopyroxene		
n:		5	9	11	4	5		4	9
$T_{Al\,it}$		1001	1029	753	761	700		1001	1029
SiO_2		40·56	41·03	40·79	40·87	40·73		57·17	57·58
TiO_2		0·04	0·05	0·05	0·05	n.a.		0·10	0·07
Al_2O_3		0·02	0·02	0·02	0·02	0·02		1·00	0·97
Cr_2O_3		0·07	0·07	n.a.	0·09	n.a.		0·34	0·37
FeO		11·31	8·64	10·08	9·60	8·70		6·95	5·32
MnO		0·14	0·13	0·21	0·17	0·19		0·16	0·14
MgO		48·09	50·98	49·59	49·93	50·64		34·09	35·68
CaO		0·03	0·04	0·03	0·05	0·06		0·42	0·39
NiO		0·33	0·38	0·35	0·36	0·34		0·09	0·09
Na_2O		0·02	0·02	0·01	0·02	0·01		0·09	0·07
K_2O		n.a.	n.a.	n.a.	n.a.	n.a.		n.a.	n.a.
Total		100·6	100·8	100·8	100·5	100·6		100·3	100·5
Mg#		88·3	91·3	89·7	90·3	91·2		89·6	92·3
	LOQ						LOQ		
Li	0·08	2·16	2·04	2·79	2·68	2·42	0·08	1·32	1·24
Na*	5·95	47	52	20	23	16	n.a.	n.a.	n.a.
Al*	7·70	27	32	3	5	2	n.a.	n.a.	n.a.
P*	2·56	41	43	13	13	12	n.a.	n.a.	n.a.
Ca*	9·09	136	145	84	79	102	n.a.	n.a.	n.a.
Sc*	0·10	1·32	1·24	1·58	1·61	2·16	0·11	6·10	4·33
Ti	0·81	150	23	27	52	25	0·86	665	107
V*	0·07	5·4	4·6	1·4	2·8	1·3	0·03	65·8	60·5
Cr*	0·60	104	129	28	35	29	0·65	2861	2987
Mn*	0·29	1160	1049	1599	1383	1568	0·44	1259	1018
Co*	0·19	149	149	143	143	121	0·07	59	57
Ni*	0·57	2600	3165	2934	2812	2684	0·09	689	825
Cu	0·08	1·04	1·06	0·19	0·35	0·10	0·09	0·82	1·66
Zn*	0·85	86	81	146	117	140	0·31	62	48
Ga*	0·10	0·125	0·149	0·099	0·093	0·048	0·055	5·1	2·5
Rb	0·033	0·014	0·017	0·030	0·007	0·019	0·035	0·045	0·044
Sr	0·007	0·0070	0·0089	0·0072	0·0093	0·0147	0·008	0·1350	0·3469
Y	0·002	0·0059	0·0069	0·0116	0·0091	0·0114	0·003	0·0990	0·1226
Zr	0·007	0·26	0·41	0·26	0·10	0·25	0·007	0·82	0·86
Nb	0·002	0·23	0·28	0·73	0·21	0·79	0·003	0·08	0·17
Mo	0·024	0·035	0·036	0·065	0·052	0·040	0·022	0·043	0·041
Cd		n.a.	n.a.	n.a.	n.a.	n.a.	0·040	0·080	0·155
In	0·003	0·0079	0·0078	0·0194	0·0075	0·0195	0·003	0·0111	0·0091
Ba	0·019	0·151	0·073	0·071	0·027	0·049	0·019	0·19	0·29
La	0·001	0·0017	0·0027	0·0027	0·0008	0·0027	0·001	0·0153	0·0164
Ce	0·001	0·0042	0·0020	0·0028	0·0029	0·0053	0·002	0·057	0·065
Pr	0·001	0·0006	0·0010	0·0007	0·0004	0·0017	0·001	0·0091	0·0101
Nd	0·005	0·0019	0·0026	0·0022	0·0017	0·0070	0·006	0·051	0·054
Sm	0·007	0·0027	0·0046	0·0036	0·0016	0·0046	0·007	0·020	0·023
Eu	0·002	0·0014	0·0011	0·0015	0·0005	0·0013	0·002	0·0067	0·0088
Gd	0·011	0·0028	0·0048	0·0057	0·0024	0·0052	0·011	0·025	0·027
Tb	0·001	0·0005	0·0004	0·0009	0·0005	0·0010	0·001	0·0040	0·0048
Dy	0·007	0·0017	0·0025	0·0029	0·0020	0·0029	0·007	0·024	0·030
Ho	0·002	0·0004	0·0012	0·0010	0·0011	0·0013	0·002	0·0049	0·0055
Er	0·006	0·0015	0·0017	0·0026	0·0025	0·0029	0·006	0·0142	0·0153
Tm	0·002	0·0005	0·0008	0·0010	0·0007	0·0007	0·002	0·0020	0·0025
Yb	0·008	0·0022	0·0030	0·0055	0·0054	0·0066	0·008	0·0152	0·0157
Lu	0·001	0·0004	0·0006	0·0014	0·0012	0·0013	0·001	0·0021	0·0022
Hf	0·003	0·0082	0·0105	0·0072	0·0065	0·0050	0·003	0·043	0·042
Ta	0·002	0·071	0·037	0·044	0·011	0·059	0·001	0·008	0·031
Pb	0·004	0·150	0·090	0·090	0·142	0·159	0·004	0·131	0·065
Th	0·0008	0·0008	0·0008	0·0008	0·0003	0·0013	0·001	0·0037	0·0031
U	0·0008	0·0014	0·0016	0·0021	0·0002	0·0008	0·002	0·0031	0·0021

(continued)

with veining related to kimberlite infiltration, and can show weak to marked pleochroism.

Spinel (chromite) is often, but not exclusively associated with phlogopite or cpx and may also occur as ovoid inclusions in olivine. In some xenoliths, discrete, roundish spinel grains and inclusions are distributed throughout. A third type of anhedral, small spinel grains is probably associated with melt infiltration.

Sulphide occurs in most xenoliths, either included in olivine or other primary silicates, or interstitially.

Table 2: Continued

Rock type:		ph-lh	lh	ph-wehr		ph-lh/hz	ph-wehr	Tikiusaaq
n:		5	9	8		5	7	
$T_{Al\ it}$		1001	1029	753		1001	753	
SiO_2	Clinopyroxene	54·39	54·40	54·99	Phlogopite	39·78	41·63	Kimberlite
TiO_2		0·24	0·20	0·11		1·20	0·25	
Al_2O_3		2·15	1·78	0·26		12·72	10·74	
Cr_2O_3		1·56	1·45	1·32		0·90	0·25	
FeO		3·18	2·64	2·50		4·28	3·76	
MnO		0·11	0·10	0·09		0·04	0·10	
MgO		16·11	16·84	16·85		23·80	25·81	
CaO		20·36	20·75	22·38		0·14	0·11	
NiO		0·05	0·07	0·06		0·20	0·22	
Na_2O		1·79	1·53	1·20		0·37	0·38	
K_2O		0·09	0·03	0·03		9·85	10·03	
Total		100·0	99·7	99·9		93·7	93·1	
Mg#		90·0	91·8	92·2		90·9	92·5	
	LOQ				LOQ			
Li	0·11	1·29	1·25	1·75	0·14	1·84	2·51	35
Na*		n.a.	n.a.	n.a.	n.a.	n.a.	n.a.	
Al*	n.a.	n.a.	n.a.	n.a.	n.a.	n.a.	n.a.	
P*	n.a.	n.a.	n.a.	n.a.	n.a.	n.a.	n.a.	
Ca*	6·89	n.a.	n.a.	n.a.	9·95	n.a.	n.a.	
Sc*	0·15	45	31	176	0·16	3·4	2·2	21
Ti	1·27	1463	1155	605	1·46	7203	2154	
V*	0·05	354	252	288	0·05	167	38	216
Cr*	0·99	11483	10003	10487	0·95	6028	1893	723
Mn*	0·70	801	664	774	0·68	214	179	1486
Co*	0·15	21	19	18	0·16	48	46	75
Ni*	0·17	321	381	306	0·18	1447	1350	549
Cu	0·12	1·14	1·86	0·91	0·13	0·36	0·45	80
Zn*	0·46	16	13	17	0·46	48	50	75
Ga*	0·09	7·0	3·8	2·5	0·09	261	244	6
Rb	0·05	0·13	0·21	0·34	0·07	360	185	46
Sr	0·018	150	176	263	0·018	19·4	5·0	2065
Y	0·004	2·8	3·7	7·1	0·004	0·0761	0·0939	32
Zr	0·013	39	51	73	0·013	2·6	1·4	583
Nb	0·005	0·29	0·29	0·64	0·005	6·6	12·2	226
Mo	0·035	0·028	0·039	0·093	0·071	0·037	0·034	0·92
Cd	0·066	0·31	0·29	0·66	0·071	0·049	0·099	0·49
In	0·007	0·069	0·039	0·305	0·007	0·0117	0·0147	
Ba	0·031	0·48	0·48	1·03	0·089	1098	909	833
La	0·002	3·46	3·01	4·95	0·003	0·024	0·056	236
Ce	0·004	13	14	20	0·003	0·038	0·089	526
Pr	0·002	2·0	2·1	3·3	0·002	0·0044	0·0108	55
Nd	0·010	9·8	11·2	17·0	0·009	0·012	0·042	199
Sm	0·013	2·2	2·9	4·2	0·015	0·0048	0·0145	26
Eu	0·004	0·66	0·88	1·31	0·007	0·017	0·022	6·7
Gd	0·017	1·7	2·4	3·6	0·044	0·020	0·047	16
Tb	0·002	0·19	0·30	0·44	0·002	0·0007	0·0013	2·1
Dy	0·010	0·91	1·39	2·29	0·010	0·0015	0·0080	8·5
Ho	0·002	0·13	0·18	0·33	0·003	0·0006	0·0021	1·2
Er	0·009	0·26	0·31	0·68	0·010	0·0022	0·0061	2·6
Tm	0·003	0·03	0·04	0·07	0·002	0·0007	0·0008	
Yb	0·013	0·17	0·16	0·37	0·013	0·0023	0·0050	1·7
Lu	0·002	0·02	0·02	0·04	0·002	0·0004	0·0008	0·23
Hf	0·005	2·2	2·9	4·1	0·006	0·1027	0·0660	13
Ta	0·003	0·038	0·059	0·107	0·003	0·58	0·78	12
Pb	0·006	0·293	0·253	0·363	0·006	0·27	0·40	5·3
Th	0·003	0·065	0·042	0·040	0·002	0·0241	11·1	21
U	0·001	0·019	0·012	0·026	0·001	0·010	0·493	5·3

*Elements analysed by medium resolution in olivine.

Medians rather than means were taken to decrease the sensitivity to outlying values. dun, dunite; hz, harzburgite; lh, lherzolite; perid, peridotite; ph, phlogopite; wehr, wehrlite. Mg# is 100Mg/(Mg + Fe) molar; n.a., not analysed or not available (below detection). Tikiusaaq kimberlite from Tappe *et al.*, (2017), plus Li and Zn from Howarth *et al.* (2011); La, Ce, Ga, Cu and Mo from Kjarsgaard *et al.* (2009; Ekati); Cd from Eccles *et al.* (2004; Alberta). $T_{Al\ it}$, Al-in-olivine temperature (de Hoog *et al.*, 2010) calculated iteratively with the regional geothermal gradient, as in Table 1.
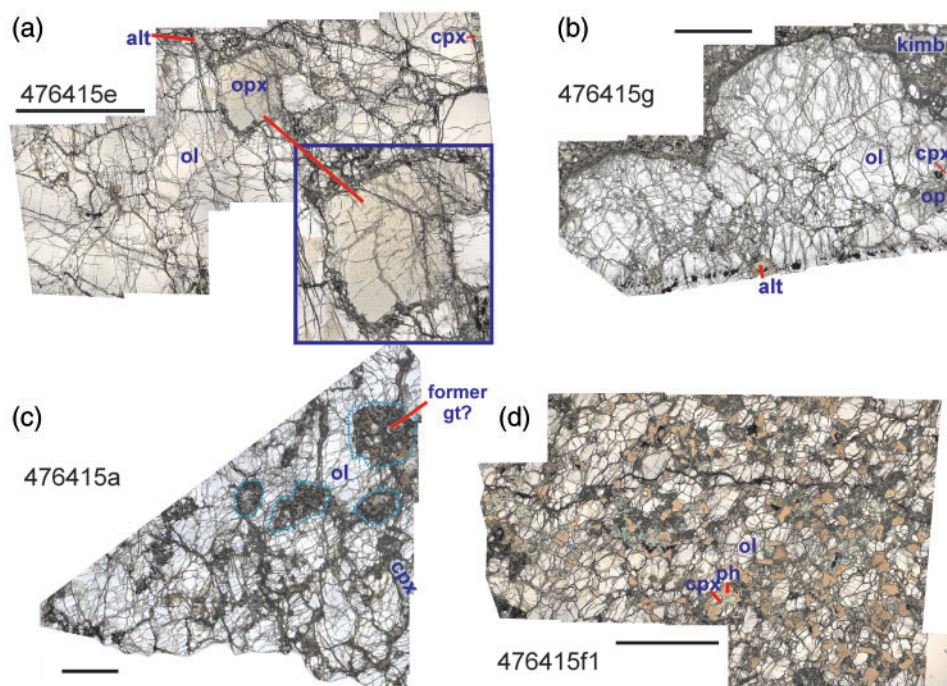
Fig. 2. Representative thick section photographs of mantle xenoliths recovered from Pyramidefjeld and Midternaes (plane-polarized light), showing (a, b) lherzolite, (c) phlogopite-lherzolite and (d) phlogopite-wehrlite. The texturally equilibrated appearance of phlogopite and cpx in (d) should be noted. In (a) the inset shows enlarged opx with exsolution lamellae. In (c) the outlines of suggested former grains of garnet, now filled with spinel plus a felty mass of presumably former pyroxene, are highlighted with dotted lines. Clinopyroxene generally has a minty green colour, whereas a mossy green colour is exhibited by microcrystalline alteration patches. Scale bar represents 5 mm. alt, alteration; gt, garnet; cpx, clinopyroxene; kimb, kimberlite; ol, olivine; opx, orthopyroxene; ph, phlogopite.

In addition, small irregular sulphide grains are ubiquitous in the otherwise cryptocrystalline grain boundary component. Their composition was not analaysed.

Roundish aggregates with relatively well-defined boundaries and consisting of abundant spinel plus a felty mass of, presumably, altered pyroxene appear to replace former garnet grains, as observed in three lherzolites and a harzburgite (476407a, 476415a, 476415h1, 476424b; Fig. 3f).

Major and trace elements
Median major and trace element analyses for minerals grouped by lithology are given in Table 2; the full dataset without statistical evaluation is given in Supplementary Data Electronic Appendices 3 and 4, whereas Appendices 5–8 show trace element abundances with instrumental standard deviations reflecting counting statistics, and standard deviations for multiple measurements per grain ($n = 3$ when grain size permitted) and for multiple grains per sample, allowing assessment of intra-grain and inter-grain homogeneity.

Olivine
Olivine in lherzolites has Mg# $[100Mg/(Mg + Fe^{total})$ molar] and NiO contents ranging from 88·1 to 91·3 and 0·34 to 0·38 wt %, respectively (Fig. 4a). Olivine in phl-wehrlites has indistinguishable Mg# (88·7–91·9), with NiO contents ranging to lower values (0·30–0·37 wt %).

Olivine in wehrlites is characterized by a conspicuous offset to higher MnO at a given Mg# compared with olivine in lherzolites (Fig. 4b), and also has lower median Na (20 vs 52 ppm), Al (3·5 vs 32 ppm), P (13 vs 43 ppm), Ca (84 vs 145 ppm), Cr (28 vs 129 ppm), V (1·4 vs 4·6 ppm) and Cu contents (0·2 vs 1·1 ppm), whereas Li, Sc, Mo and In contents are higher (Table 2 and Fig. 4). It should be noted that some of the Al concentrations are below the average LOQ of 7·70 ppm. Olivine in three of four phl-lherzolites (476415a, 476415o, 476415r) is characterized by low Mg# (87·5–88·3), NiO contents (0·29–0·33 wt %) and MnO contents (0·14–0·27 wt %) compared with those in the phlogopite-free variety (median 91·3, 0·38 wt % and 0·13 wt %), but otherwise has similar trace element contents. A fourth sample (476424q) has lower Cu, Na, P and V and higher Li contents than lherzolitic olivine, more akin to wehrlitic olivine. Much larger Cu variations are observed for olivine in the two lherzolite groups than in other peridotite types.

With the exception of one sample, which has an elevated MnO content for its Mg#, olivine in dunites is indistinguishable from that in lherzolites with respect to major elements, V and Sc contents, but it plots with phl-wehrlites in terms of other trace elements (Na, Al, Cu, Mo). Olivine in phl-dunite and -harzburgite has the lowest Mg# (85·7 and 87·1, respectively) and NiO contents (0·27 and 0·32 wt %, respectively) (Fig. 4a). Olivine in
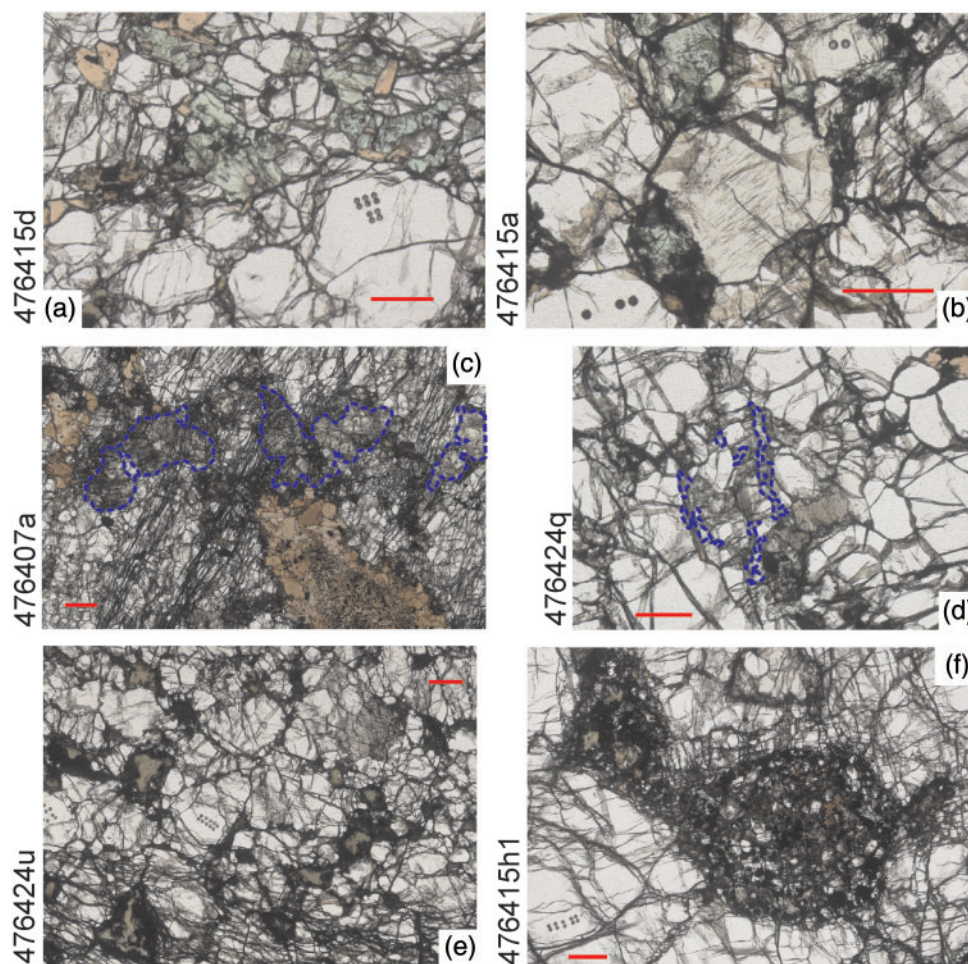
Fig. 3. Thick sections in plane-polarized light illustrating various petrographic features. (a) Multiple sizes and shapes of olivine in a single sample (phl-wehrlite 476415d). (b) Large, subhedral opx grains with lobate grain boundaries and exsolution lamellae (phl-lherzolite 476415a). (c) Opx distributed as strings of grains, highlighted with dashed lines (phl-harzburgite 476407a, also containing a large phlogopite cluster). (d) Small, anhedral cpx (highlighted with dashed lines) rimming opx and olivine (phl-lherzolite 476424q). (e) Microcrystalline green mass filling out well-defined subhedral grain shapes interpreted as former pyroxene(s) (peridotite 476424u). (f) Roundish aggregate with relatively well-defined boundary, consisting of spinel plus a felty mass of presumably former pyroxene, possibly the breakdown products of former garnet grains (lherzolite 476415h1). Scale bar represents 1 mm; laser pits are visible in some of the grains.

phl-dunite, -harzburgite and -lherzolite has low MnO at a given Mg#, but P, Cu, Na and Al abundances similar to phlogopite-free counterparts. Olivine in the phlogopite-free wehrlite (476414d) is similar to both phl-wehrlites and phl-lherzolites, and it is possible that phlogopite and/or opx are absent as a result of sectioning effects. Both phlogopite-free and phl-peridotites with possible altered pyroxenes have olivine with high MnO contents at a given Mg#, which characterizes the wehrlite suite. Overall, the entire sample suite shows a weak positive correlation between Mg# and NiO, and a negative correlation with MnO (Fig. 4a and b).

Orthopyroxene (opx)
Lherzolitic opx has Mg# from 90·6 to 93·4, TiO_2 from 0·04 to 0·1 wt %, Al_2O_3 from 0·84 to 1·2 wt %, Cr_2O_3 from 0·34 to 0·93 wt % and CaO from 0·32 to 0·68 wt %. As for coexisting olivine, opx in three of four phl-lherzolites has homogeneously lower Mg# (89·5–89·7), and two of

these have the highest TiO_2 contents in the sample set (0·12 and 0·13 wt %) (Fig. 5a). They also have some of the highest Na_2O, Al_2O_3 and Mn contents (Fig. 5b–d). Like the olivine it coexists with, opx in a single phl-harzburgite has low Mg# (88·8) and is otherwise similar to that in three of the phl-lherzolites. In contrast, opx in phl-lherzolite 476424a is similar to that in the phlogopite-free lherzolites. For the entire suite, Mg# in opx correlates negatively with TiO_2, Mn (Fig. 5a and d), Zn and Ga (not shown).

Clinopyroxene (cpx)
Clinopyroxene in lherzolites has Mg# from 89·8 to 93·6, which is negatively correlated with TiO_2, which ranges from 0·02 to 0·66 wt % (Fig. 6a). As is true for coexisting olivine and opx, cpx in three of the phl-lherzolites has some of the lowest Mg# and highest TiO_2 contents in the sample suite, whereas cpx in the other two phl-lherzolites has high Mg# and low TiO_2, more similar to
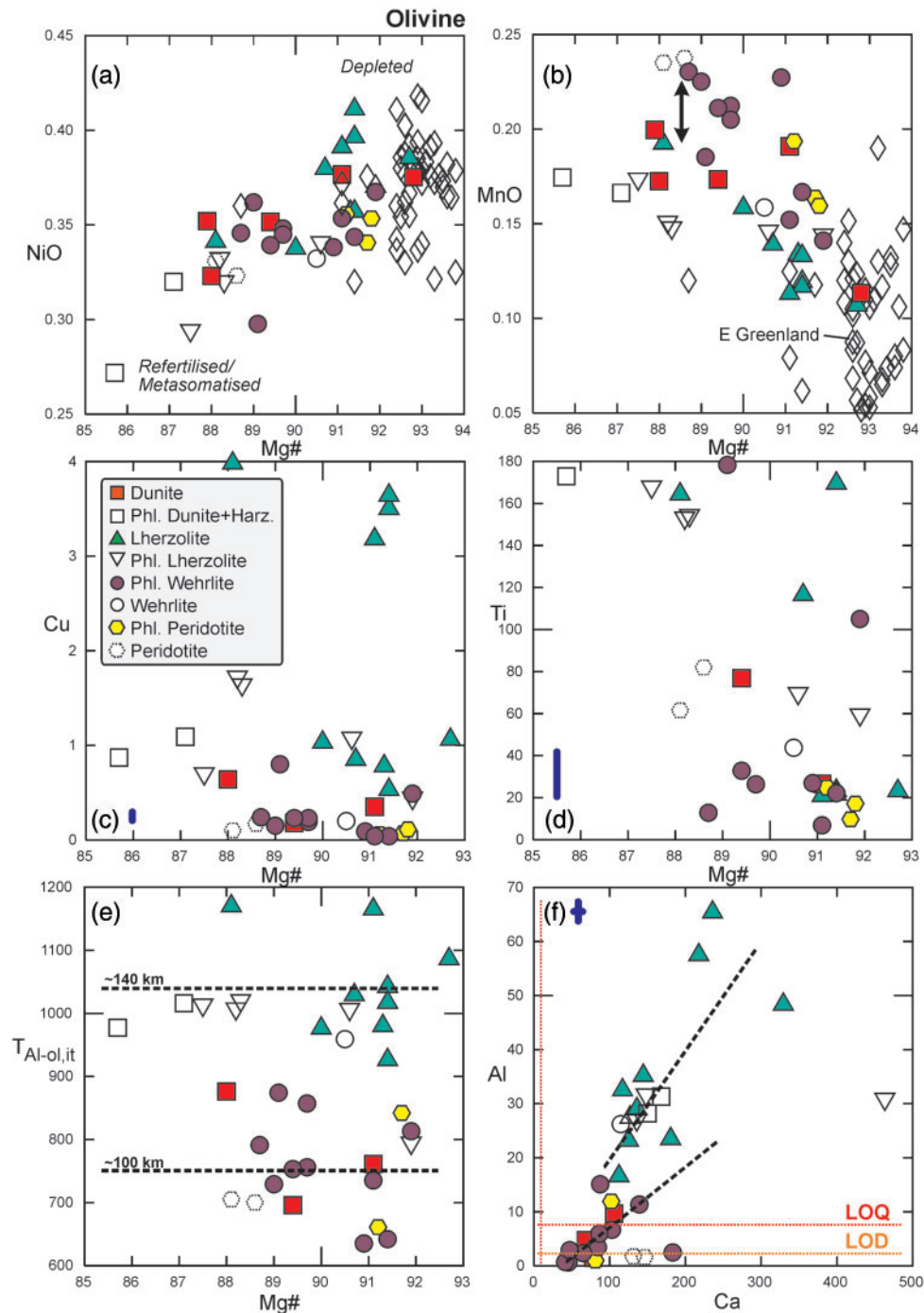
Fig. 4. Minor and trace elements (oxides in wt %, others in ppm) in olivine (a–d) and Al-in-olivine temperature solved iteratively with the regional geothermal gradient ($T_{Al-ol, it}$) (e) as a function of Mg# [100Mg/(Mg + Fe) molar]. (f) Ca vs Al abundances. The incorporation of many of these trace elements is temperature-dependent (Witt-Eickschen & O'Neill, 2005; De Hoog *et al.*, 2010). Shown for comparison in (a) and (b) are opx from highly depleted eastern Greenland xenoliths (open diamonds; Bernstein *et al.*, 1998). In (b) the offset to higher MnO content at a given Mg# in cpx from phl-wehrlites and pyroxene-free peridotites compared with lherzolites and dunites should be noted. Two dashed lines in (e) represent the median temperatures calculated for lherzolites and phl-wehrlites, respectively, which have been inverted for depth, as given. In (f) the more strongly increasing Al contents at a given Ca content in lherzolitic compared with wehrlitic cpx should be noted. Also shown in (c), (d) and (f) are average standard deviations for multiple analyses per sample (bars next to panel labels), and in (f) the average limit of quantification (LOQ; vertical and horizontal dotted lines), with most wehrlites having Al abundances below the LOQ but above the LOD (limit of detection; dotted line).

that in phlogopite-free lherzolites. Clinopyroxene in phl-wehrlites has higher median Mg# than lherzolitic cpx (92·2 vs 91·8), but lower and less variable TiO$_2$ contents ranging from 0·07 to 0·14 wt %. Clinopyroxene in phl-wehrlites is

characterized by highly variable CaO/Al$_2$O$_3$ (31–114), whereas this ratio is lower and varies less (from nine to 14) in lherzolitic cpx (Fig. 6b), reflecting compositions from nearly pure diopside to a small jadeite component
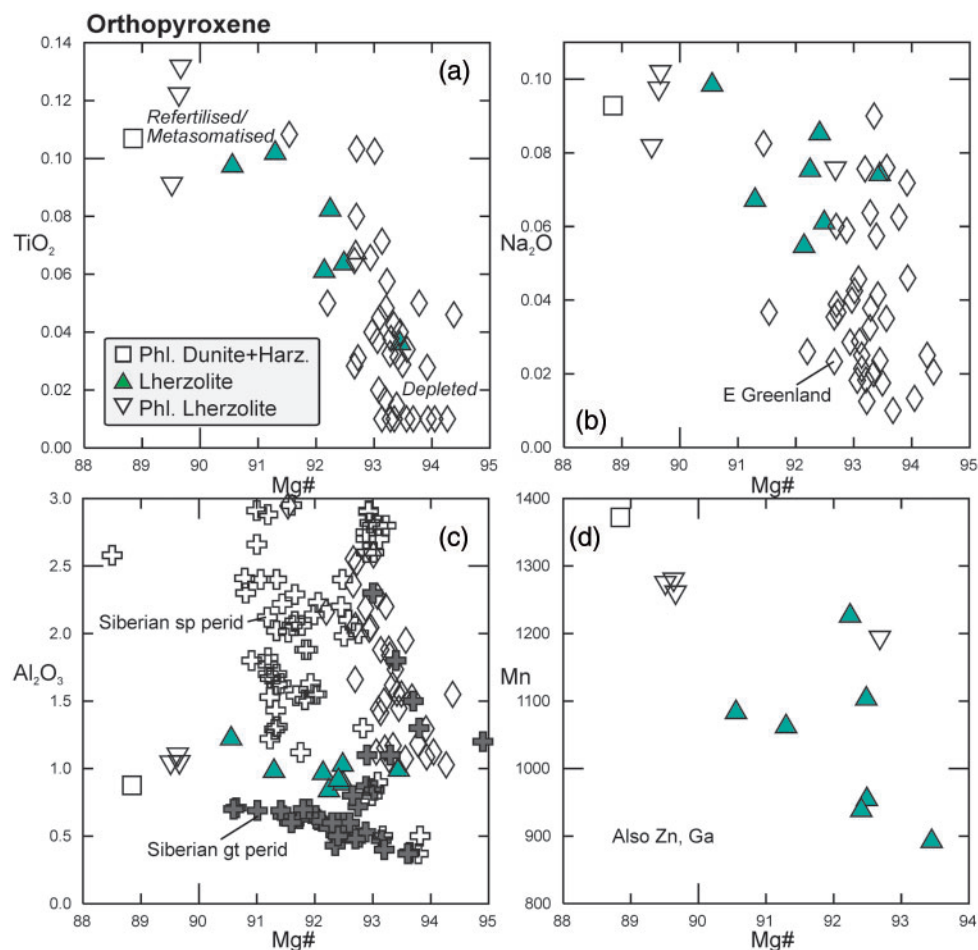
Fig. 5. Major, minor and trace elements (oxides in wt %, others in ppm) in opx (a–d) as a function of Mg# [100Mg/(Mg + Fe) molar]. Shown for comparison in (a), (b) and (c) are opx from highly depleted eastern Greenland xenoliths (open diamonds; Bernstein *et al.*, 1998); in (c) opx in spinel (open crosses) and garnet peridotites (filled crosses) from Siberia (Ionov *et al.*, 2006; Doucet *et al.*, 2012; Howarth *et al.*, 2014) are shown to illustrate the difference in Al_2O_3 contents between the two mineralogies, with opx from SW-GNAC (this study) falling between the two.

(up to 7%) with very little Tschermaks (up to 2%). MnO in wehrlite does not show the marked offset to higher values at a given Mg# exhibited by olivine.

Wehrlitic cpx shows an anti-correlation of Mg# with Cd and In (Fig. 6c and d) and, compared with lherzolitic cpx, is characterized by lower median Na_2O (1·2 vs 1·5 wt %), Al_2O_3 (0·3 vs 1·8 wt %), Cu (0·9 vs 1·9 ppm) and Ga (2·5 vs 3·8 ppm) abundances, but higher median Li (1·7 vs 1·3 ppm), Sc (176 vs 31 ppm), Zn (17 vs 13 ppm), Sr (263 vs 176 ppm), Y (7·1 vs 3·7 ppm), Zr (73 vs 51 ppm), Nb (0·64 vs 0·29 ppm), Mo (0·09 vs 0·04 ppm), Cd (0·66 vs 0·29 ppm), In (0·31 vs 0·04 ppm), Ba (1·0 vs 0·5 ppm) and total rare earth element (REE) contents (58 vs 37 ppm). With regard to these trace elements, cpx in phl-lherzolites is more similar to that in lherzolites than to that in phl-wehrlites. Although the REE patterns of lherzolitic and phl-wehrlitic cpx overlap, several of the former have lower REE contents and a few show stronger heavy REE (HREE) depletion with steeper negative slopes in the middle REE (MREE), whereas some of the latter are more strongly REE-enriched, with higher Nd/La (Fig. 7).

Phlogopite
Even though phlogopite in wehrlites compared with dunites and lherzolites does not form consistently different groups, the former has lower median TiO_2 (0·25 vs 1·20 wt %) and Al_2O_3 (10·7 vs 12·7 wt %) contents, but higher Li (2·5 vs 1·8 ppm), Nb (12·2 vs 6·6 ppm), Th (11·1 vs 0·02 ppm) and U (0·49 vs 0·01 ppm) abundances. Phlogopite in two samples (476415b2o and 476415c) has very low Mg# (86·9 and 87·5) and is conspicuously enriched in TiO_2, Li, Sr and Zr (Fig. 8), with low Ba and Th abundances.

Spinel
Spinel was analysed in six of the samples, five of which are opx-bearing and two of which are phlogopite-bearing. It is Cr_2O_3-rich (chromite) has Mg# ranging from 36·3 to 53·9, Cr# from 73·2 to 90·4 and Fe^{3+}# [molar $Fe^{3+}/(Fe^{3+} + Fe^{2+})$], determined from stoichiometry after Droop (1987), from 26·6 to 39·9. The highest value of each is recorded for the single dunite (476415i). Trace elements were not determined.
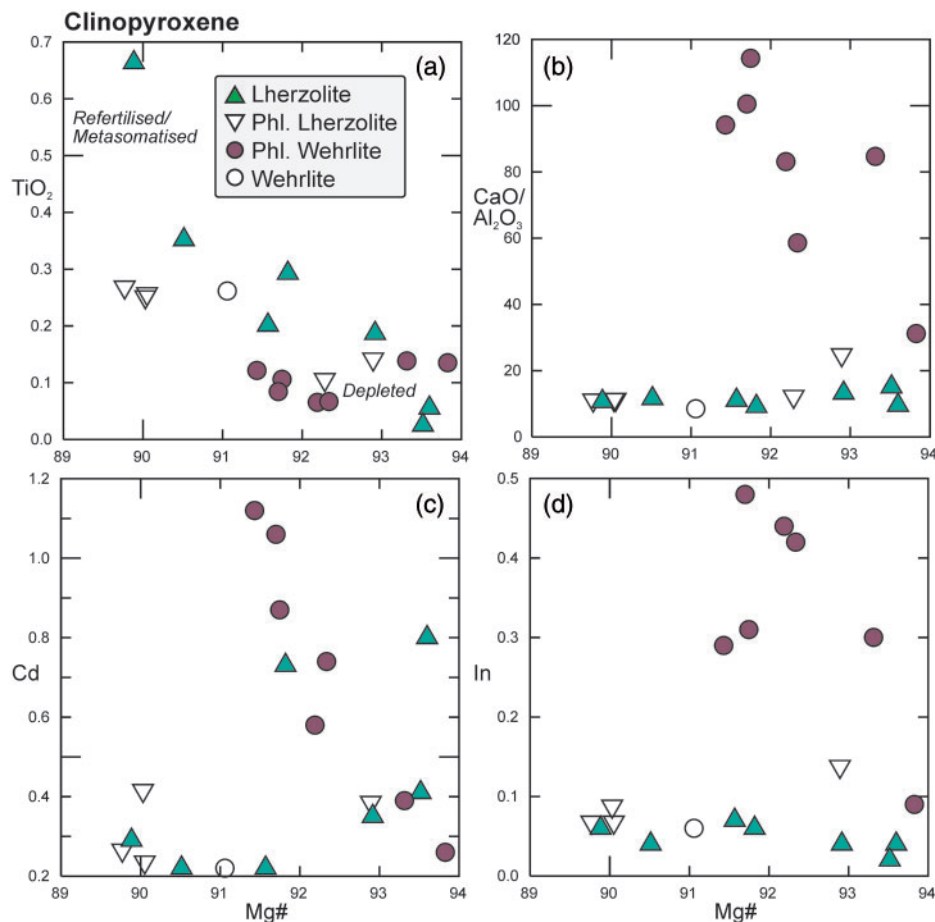
Fig. 6. Major, minor and trace elements (oxides in wt %, others in ppm) in cpx as a function of Mg# [100Mg/(Mg + Fe) molar].

Radiogenic isotopes

Clinopyroxene in four samples (phl-wehrlite 476414a, lherzolites 476415b, 476415g and 476424b) has relatively homogeneous measured $^{87}Sr/^{86}Sr$ (0·703753 ± 0·000082; 2σ) and $^{143}Nd/^{144}Nd$ (0·512851 ± 0·000006) (Table 3). Parent–daughter ratios were calculated from elemental Rb and Sr abundances determined by LA-ICP-MS in cpx (corresponding to average $^{87}Rb/^{86}Sr$ 0·00063), and Sm and Nd were determined by isotope dilution (average $^{147}Sm/^{144}Nd = 0·147$). Using these ratios, the calculated isotopic compositions at the time of host kimberlite eruption ~150 myr ago are identical to measured values for $^{87}Sr/^{86}Sr$ and only slightly lower for $^{143}Nd/^{144}Nd$ (0·512705). The latter ratio lies between that of Bulk Silicate Earth (0·512634) and Depleted Mantle (0·5131; values of Salters & Stracke, 2004), whereas $^{147}Sm/^{144}Nd$ is lower than in both reservoirs (0·1967 and 0·2135, respectively; Blichert-Toft & Puchtel, 2010), leading to future model ages with respect to a chondritic mantle evolution and c. 1 Ga ages for a Depleted Mantle model (1·04 ± 0·27 Ga, 2σ).

GEOTHERMOBAROMETRY

Pressure–temperature estimates are given in Table 1. Following recommendations by Nimis & Grütter (2010),

temperatures for assemblages bearing two pyroxenes are estimated using the formulation of Taylor (1998; T_{TA98}) and checked for equilibrium with the Ca-in-orthopyroxene thermometer of Nimis & Grütter (T_{NG10}). We calculate temperatures at a pre-set pressure of 4 GPa, which corresponds to the middle of the pressure interval obtained from iterative solutions described below. With the exception of two samples showing a difference of ~300°C for the two thermometers (476415b2a and 476415e), pyroxenes in the lherzolites appear to be in equilibrium, giving median T_{TA98} and T_{NG09} of 944 and 935°C, respectively, similar to phl-lherzolites with 922 and 932°C, respectively.

Temperatures for clinopyroxene-free samples can be calculated using a variety of empirically formulated olivine thermometers based on Al, Cr and V, the concentrations of which appear to be independent of the concentrations in coexisting peridotite minerals (De Hoog et al., 2010; Smith, 2013). Although calibrated for garnet peridotites, Al-in-olivine (T_{Al-ol}) temperatures calculated for spinel peridotites generally show good agreement with pyroxene-based temperatures (De Hoog et al., 2010). At 4 GPa, median T_{Al-ol} for lherzolites and phl-lherzolites is 1012 and 989°C, respectively, somewhat higher than pyroxene-based temperatures, but 795°C for phl-wehrlites, 804°C for dunites and 747°C
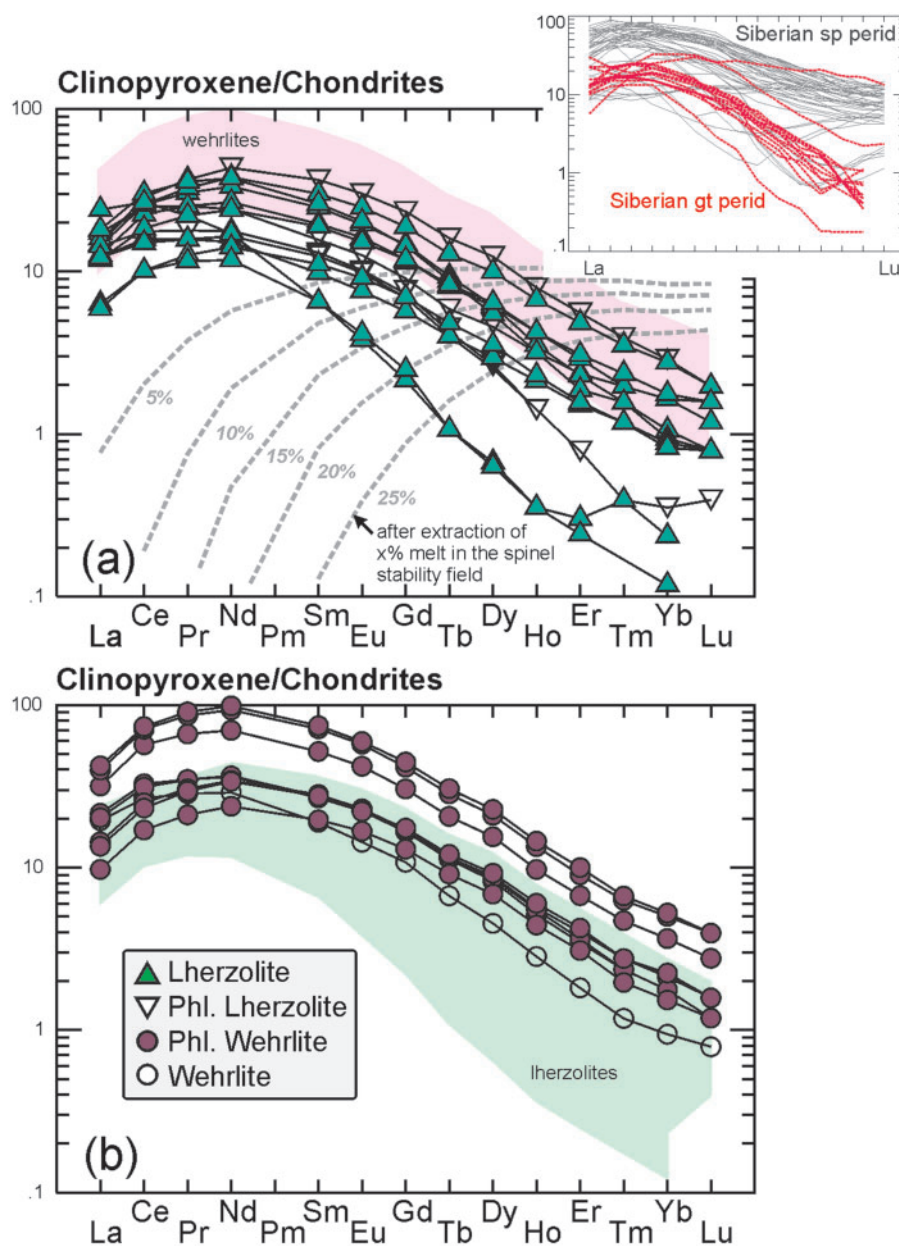
Fig. 7. Chondrite-normalized REE patterns of cpx. Shown for comparison in (a) are patterns for cpx after melt extraction in the spinel stability field from McCoy-West et al. (2015) (grey dashed lines; numbers give percentage of melt extraction). Inset in (a) shows patterns for cpx in spinel and garnet peridotites from Siberia (references are given in Fig. 5 caption), illustrating the distinct abundances and slopes, in particular in the MREE–HREE, for these two lithologies. Chondrite normalization after Sun & McDonough (1989).

for peridotites inferred to contain altered pyroxene. It should be noted that Al abundances in the low-temperature samples are in many cases below the LOQ, but mostly above the LOD (limit of detection).

In the absence of garnet, there is no suitable geobarometer to obtain independent pressure estimates for the samples investigated here. Data for garnet lherzolites from the same kimberlite localities were obtained previously, using conventional ion exchange thermobarometry, and yielded temperatures of ∼900–1150°C at pressures of ∼3·5–6·5 GPa (Nielsen et al., 2008). The geothermal gradient obtained for that suite is equivalent to an ∼42–44 mW m^{-2} surface heat flow (Nielsen et al., 2008). To co-locate the samples in the present study in the lithosphere column, $T_{Al\text{-}ol}$ was solved iteratively with a geothermal gradient of 42 mW m^{-2}, which assumes that the samples have equilibrated to the geotherm and that temperatures are not
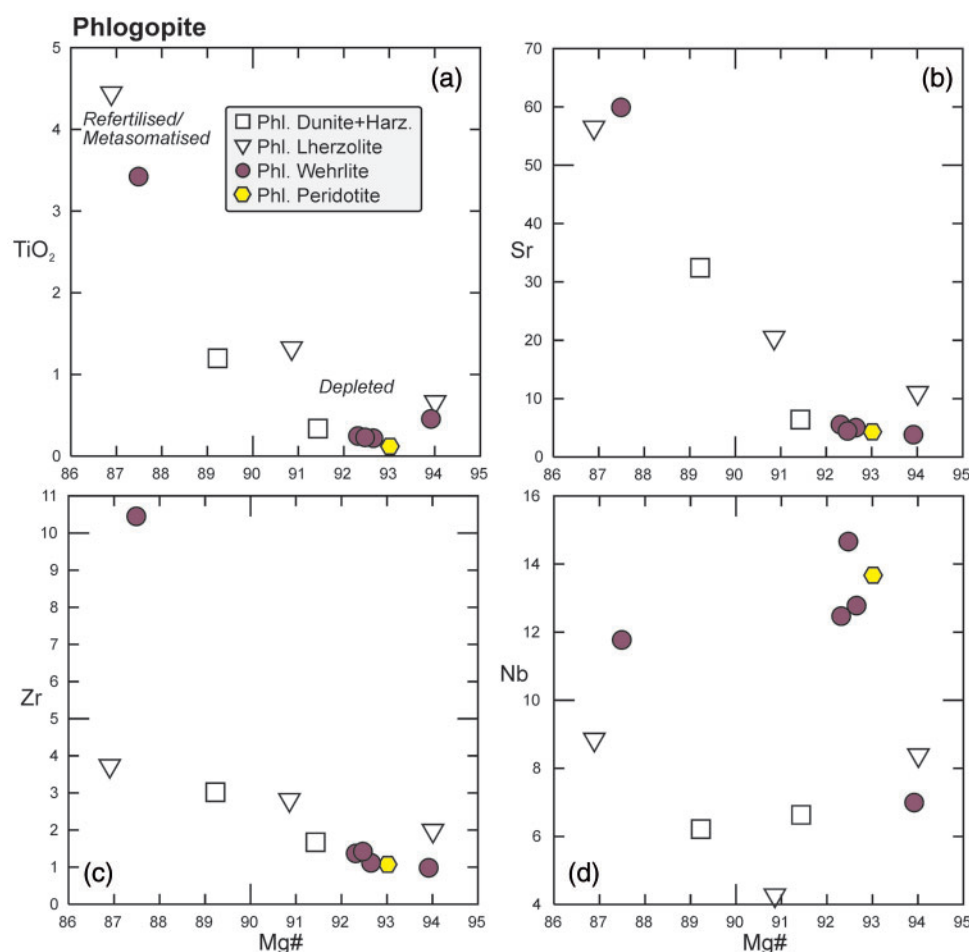
Fig. 8. Major and trace element relationships (oxides in wt %, others in ppm) in phlogopite as a function of Mg# [100Mg/(Mg + Fe) molar].

related to temperature excursions (e.g. high temperature compared with the ambient geotherm owing to transient heating). The resultant temperatures are somewhat higher than those calculated at 4 GPa, with correspondingly higher pressure estimates, for lherzolites (1036°C and 4·5 GPa) and phl-lherzolites (1001°C and 4·2 GPa), but lower for phl-wehrlites (753°C and 3·0 GPa), dunites (761°C and 3·0 GPa) and pyroxene-free peridotites (702°C and 2·8 GPa), thus confirming their relative positions in the lithosphere, as inferred from calculations at a preset pressure.

TRACE ELEMENT PARTITIONING AND ASSESSMENT OF EQUILIBRIUM

To assess compositional equilibrium between the minerals, we calculate apparent distribution coefficients $^{\text{Mineral 1/Mineral 2}}D_{\text{Element}}$ for different mineral pairs (Table 4). The pairs are grouped according to lithology to account for compositional effects and also temperature effects related to the lower average temperatures of last equilibration recorded in wehrlites and peridotites compared with lherzolites and harzburgites (see previous section). Results

for selected elements are visualized in Supplementary Data Electronic Appendix 9. It is particularly interesting to test whether cpx and phlogopite, which show evidence for textural equilibration but are frequently added during modal metasomatism (O'Reilly & Griffin, 2013; Pearson & Wittig, 2014), are in trace element equilibrium with olivine and opx, which may represent the original residual assemblage after partial melt extraction.

Lherzolites represent the only two-pyroxene-bearing lithologies in the sample suite. Many trace elements strongly prefer cpx with $^{\text{opx/cpx}}D_{\text{Element}} < 0.5$, except for Li, Mn, Cu, Ga and Mo, which partition roughly equally ($0.5 \leq {}^{\text{opx/cpx}}D_{\text{Element}} \leq 2$), and Co, Ni and Zn, which have a stronger preference for opx. Median calculated $^{\text{opx/cpx}}D_{\text{Element}}$ values for five phlogopite-bearing and eight phlogopite-free varieties are generally similar, except for higher $D_{\text{Ti, MREE}}$ and lower $D_{\text{Zr, Hf}}$ for the former (D_{LREE}, where LREE is light REE, was not determined because of low concentrations in opx and susceptibility to kimberlite contamination). Trace element equilibrium for lherzolites is consistent with coincident (within the uncertainty of ∼70°C; Nimis & Grütter, 2010) temperatures derived from two-pyroxene thermometry, which

Table 3: Sr–Nd isotope systematics and model ages for cpx separates

Sample	Lithology	$^{87}Rb/^{86}Sr$*	$^{87}Sr/^{86}Sr$	2SE[†]	$^{87}Sr/^{86}Sr_i$[‡]	Sm (ppm)	Nd (ppm)
476414a	phl wehr	0·0005	0·703758	0·000024	0·703757	4·1	15·7
476415b	lherz	0·0015	0·703695	0·000015	0·703692	3·6	15·1
476415g	lherz	0·0001	0·703790	0·000013	0·703790	3·0	12·6
476424b	lherz	0·0005	0·703771	0·000020	0·703770	1·6	6·9

Sample	$^{147}Sm/^{144}Nd$	$^{143}Nd/^{144}Nd$	2SE[†]	$^{143}Nd/^{144}Nd_i$[‡]	$\varepsilon_{Nd, i}$[§]	Uncertainty[§]	T_{DM}[¶]	T_{CHUR}[¶]
476414a	0·157	0·512854	0·000013	0·512697	4·97	0·25	1230	−231
476415b	0·145	0·512852	0·000028	0·512708	5·18	0·55	981	−206
476415g	0·145	0·512847	0·000026	0·512702	5·07	0·52	1004	−191
476424b	0·141	0·512852	0·000015	0·512712	5·25	0·30	928	−203

*Calculated from LA-ICP-MS concentrations.
[†]Analytical uncertainty (standard error).
[‡]Initial ratio calculated for time of kimberlite emplacement (152 Ma), using $\lambda^{87}Rb = 1·40 \times 10^{-11}$ (Minster & Allègre, 1980) and $^{147}Sm = 6·54 \times 10^{-12}$ (Lugmair & Marti, 1978).
[§]Per 10 000 deviation from chondritic mantle (CHUR), values from Hamilton *et al*. (1983), calculated for initial $^{143}Nd/^{144}Nd$, with uncertainty for propagated 2SE of $^{143}Nd/^{144}Nd$.
[¶]Depleted mantle (DM) of Blichert-Toft & Puchtel (2010); Chondritic Uniform Reservoir (CHUR) of Hamilton *et al*. (1983).

Table 4: Median apparent distribution cofficients for various mineral pairs grouped according to lithology

Element	Li	Sc	Ti	V	Cr	Mn	Co	Ni	Cu	Zn	Ga	Y
Olivine–phlogopite D												
ph-lh (3)	1·53	0·54	0·017	0·034	0·015	6·17	2·8	1·92	3·49	2·4	0·0009	0·08
ph-wehr (7)	1·17	0·76	0·015	0·039	0·016	8·95	3·1	2·26	1·00	2·6	0·0003	0·11
ph-perid (3)	1·08	0·68	0·017	0·045	0·018	8·35	2·7	1·76	1·15	2·3	0·0003	0·16
ph-lh/ph-perid	*1·4*	*0·8*	*1·0*	*0·8*	*0·8*	*0·7*	*1·0*	*1·1*	*3·0*	*1·1*	*2·8*	*0·5*
ph-wehr/ph-perid	*1·1*	*1·1*	*0·9*	*0·9*	*0·9*	*1·1*	*1·2*	*1·3*	*0·9*	*1·2*	*1·0*	*0·7*
ph-lh/ph-wehr	*1·3*	*0·7*	*1·1*	*0·9*	*0·9*	*0·7*	*0·9*	*0·9*	*3·5*	*0·9*	*2·8*	*0·8*
Olivine–cpx D												
lh (9)	1·62	0·032	0·094	0·018	0·010	1·53	7·2	8·6	1·39	5·7	0·04	0·0027
ph-lh (4)	1·84	0·030	0·099	0·015	0·008	1·53	7·4	8·6	1·15	6·5	0·02	0·0017
ph-wehr (9)	1·37	0·010	0·034	0·005	0·003	2·01	7·8	9·8	0·40	6·6	0·03	0·0015
ph-lh/lh	*1·1*	*0·9*	*1·1*	*0·8*	*0·8*	*1·0*	*1·0*	*1·0*	*0·8*	*1·1*	*0·5*	*0·6*
ph-wehr/lh	*0·8*	*0·3*	*0·4*	*0·3*	*0·3*	*1·3*	*1·1*	*1·1*	*0·3*	*1·1*	*0·8*	*0·5*
ph-wehr/ph-lh	*0·7*	*0·3*	*0·3*	*0·4*	*0·3*	*1·3*	*1·1*	*1·1*	*0·4*	*1·0*	*1·6*	*0·8*
opx–cpx D												
lh (8)	1·09	0·15	0·37	0·23	0·28	1·45	2·7	2·1	0·96	3·4	0·67	0·028
ph-wehr (5)	1·18	0·13	0·54	0·17	0·23	1·55	2·8	2·2	0·86	3·9	0·75	0·032
lh/ph-lh	*0·9*	*1·2*	*0·7*	*1·3*	*1·2*	*0·9*	*1·0*	*1·0*	*1·1*	*0·9*	*0·9*	*0·8*

Element	Zr	Mo	In	Sm	Eu	Gd	Tb	Dy	Ho	Er	Tm	Yb	Lu	Hf
Olivine–phlogopite D														
ph-lh (3)	0·10	1·72	0·77	0·70	0·03	0·12	1·20	1·10	0·96	1·26	1·15	1·80	1·70	0·08
ph-wehr (7)	0·14	2·09	1·31	0·10	0·07	0·19	0·39	0·20	0·47	0·56	1·26	1·12	1·93	0·11
ph-perid (3)	0·14	1·20	1·56	0·32	0·10	0·16	0·20	0·31	0·37	0·67	0·95	1·54	1·78	0·10
ph-lh/ph-perid	*0·7*	*1·4*	*0·5*	*2·2*	*0·3*	*0·7*	*5·9*	*3·5*	*2·6*	*1·9*	*1·2*	*1·2*	*1·0*	*0·8*
ph-wehr/ph-perid	*1·0*	*1·7*	*0·8*	*0·3*	*0·7*	*1·2*	*1·9*	*0·6*	*1·3*	*0·8*	*1·3*	*0·7*	*1·1*	*1·1*
ph-lh/ph-wehr	*0·8*	*0·8*	*0·6*	*7·2*	*0·4*	*0·6*	*3·1*	*5·5*	*2·0*	*2·3*	*0·9*	*1·6*	*0·9*	*0·7*
Olivine–cpx D														
lh (9)	0·0149	0·91	0·20	0·0026	0·0027	0·0028	0·0041	0·0037	0·0048	0·0065	0·0274	0·0168	0·0364	0·0069
ph-lh (4)	0·0083	1·42	0·11	0·0009	0·0014	0·0014	0·0014	0·0021	0·0050	0·0040	0·0228	0·0191	0·0355	0·0043
ph-wehr (9)	0·0039	0·81	0·08	0·0009	0·0009	0·0017	0·0013	0·0009	0·0029	0·0041	0·0126	0·0156	0·0339	0·0025
ph-lh/lh	*0·6*	*1·6*	*0·6*	*0·3*	*0·5*	*0·5*	*0·3*	*0·6*	*1·0*	*0·6*	*0·8*	*1·1*	*1·0*	*0·6*
ph-wehr/lh	*0·3*	*0·9*	*0·4*	*0·3*	*0·3*	*0·6*	*0·3*	*0·2*	*0·6*	*0·6*	*0·5*	*0·9*	*0·9*	*0·4*
ph-wehr/ph-lh	*0·5*	*0·6*	*0·7*	*1·0*	*0·6*	*1·2*	*0·9*	*0·4*	*0·6*	*1·0*	*0·6*	*0·8*	*1·0*	*0·6*
opx–cpx D														
lh (8)	0·042	1·06	0·27	0·016	0·016	0·022	0·032	0·025	0·038	0·046	0·058	0·081	0·12	0·033
ph-wehr (5)	0·022	1·13	0·15	0·009	0·010	0·014	0·019	0·026	0·038	0·045	0·065	0·088	0·10	0·017
lh/ph-lh	*1·9*	*0·9*	*1·8*	*1·8*	*1·6*	*1·5*	*1·6*	*1·0*	*1·0*	*1·0*	*0·9*	*0·9*	*1·1*	*2·0*

Ratios for *D* obtained for different lithologies (italics) are calculated to illustrate differences, which may be due to composition, temperature, oxygen fugacity for redox-sensitive elements and/or disequilibrium. Abbreviations as in Table 2.

depends principally on cpx composition, and Ca-in-opx thermometry, which relies solely on opx composition (Nimis & Grütter, 2010). Other than the aforementioned two samples, only a single phl-lherzolite (476415r)

shows a deviation of ∼80°C. The apparent equilibrium for divalent and trivalent elements, but higher deviation for the distribution of tetravalent elements between the two pyroxenes in phlogopite-bearing vs phlogopite-free

lherzolites may relate to slower diffusivities for trivalent ions (Cherniak & Liang, 2012) during modal metasomatism, evident in phlogopite addition.

With respect to trace element distribution between olivine and cpx, trace elements partition more strongly into cpx, with the exception of Li, Mn, Co, Ni and Zn, which prefer olivine over cpx, and Cu and Mo, which behave more or less indifferently. Calculated $^{olivine/cpx}D_{Element}$ values vary by less than a factor of two for lherzolites ($n = 9$) and phl-lherzolites ($n = 4$), including Ti, whereas much lower median D values are observed for Sc, Ti, V, Cr, Cu and the MREE in phl-wehrlites ($n = 9$) compared with lherzolites. Although this could reflect compositional disequilibrium between olivine and cpx in the phl-wehrlites, a straightforward interpretation of these differences is hampered by the temperature-dependent partitioning of some incompatible elements into olivine (De Hoog *et al.*, 2010) and by potential bulk compositional effects.

Compared with phlogopite, olivine has higher abundances of Li, Mn, Co, Ni, Cu, Zn and Mo. As is true for olivine–cpx pairs, differences between median $^{olivine/phlogopite}D_{Element}$ for phl-wehrlites ($n = 7$) and phl-lherzolites ($n = 3$) for Cu, Ga and the MREE may relate to temperature and/or composition. Distribution coefficients for pyroxene-free phl-peridotites ($n = 3$), which equilibrated at similarly low temperatures to the phl-wehrlites (see previous section), are more similar to D values determined for phl-wehrlites than for phl-lherzolites.

DISCUSSION

Mantle stratification beneath SW Greenland: link to mid-lithospheric discontinuity

The mantle beneath the eastern and northwestern GNAC (NW-GNAC) (Fig. 1) is more olivine-rich and opx-poor than that beneath most cratons and has consequently been suggested to more accurately represent the pre-metasomatic melt depletion history of Archaean lithosphere (Bernstein *et al.*, 2006; Wittig *et al.*, 2008). It has been previously recognized, based on platinum group element (PGE) and Os isotope systematics, that peridotites from the SW-GNAC are significantly less depleted than those from the NW-GNAC (Wittig *et al.*, 2010). Indeed, Figs 4 and 5 show that there is very little overlap with respect to olivine and opx Mg# between eastern Greenland and the SW-GNAC. Forsterite content in olivine, as a proxy for melt depletion and refertilization, in cpx-free harzburgites and dunites is similar to that in lherzolites and harzburgites, suggesting that the latter do not record a more refractory host rock with a more intense melt depletion origin.

The mantle lithosphere in the NW-GNAC was stratified at 590–550 Ma, with a strongly depleted shallow layer at 90–115 km depth yielding coarse-textured harzburgites and lherzolites, and a less depleted, texturally more variable deeper layer (140–215 km) yielding lherzolites and wehrlites, as reflected in the xenolith population entrained during Neoproterozoic kimberlite and ultramafic lamprophyre magmatism (Sand *et al.*, 2009). This cratonic mantle architecture is apparently absent beneath the SW-GNAC, where phl-wehrlites were derived from depths of $\sim$90–110 km (inverted from iteratively calculated pressures; Table 1) and lherzolites from depths of $\sim$100–170 km. Thus, this mantle-derived xenolith suite apparently records overall more intense metasomatism in the shallower lithosphere.

Interestingly, the phlogopite–cpx-rich wehrlites occur at depths where mid-lithospheric discontinuities (MLD) with negative velocity gradients are detected, which have been ascribed to the accumulation of seismically slow hydrous minerals and pyroxenes (Rader *et al.*, 2015; Selway *et al.*, 2015; Aulbach *et al.*, 2017). For example, 5–10% phlogopite over a depth interval of 10–20 km could produce the typically measured velocity reductions of 2–7% (Rader *et al.*, 2015). This modal amount of phlogopite is present in the wehrlites investigated here (e.g. Fig. 2d; Supplementary Data Electronic Appendix 10). These samples additionally occur over a seemingly narrow depth interval, which suggests that the lithospheric mantle beneath the SW-GNAC should show a seismic velocity reduction at $\sim$100 km depth, provided that this metasomatism is craton-wide and not restricted to kimberlite pathways. Such a negative phase does appear at $\sim$100–120 km depth and has been interpreted as the base of the lithosphere (Kumar *et al.*, 2005), but was reinterpreted as an MLD in a later study (Rader *et al.*, 2015). This reinterpretation is justified by other work (Nielsen *et al.*, 2008; this study, Table 1) showing that some xenoliths equilibrated at pressures of up to 5·5 GPa, corresponding to $\sim$170 km depth, which defines the minimum depth to the lithosphere–asthenosphere boundary.

If the lithospheric mantle beneath the SW-GNAC had a similar compositional make-up to its NW counterpart 590–550 myr ago, the different lithologies recorded in our sample suite, with strongly metasomatized rather than depleted peridotites at shallow depth, indicate that the intense metasomatic overprint recorded in our sample suite is relatively young, possibly related to early Mesozoic rifting (Tappe *et al.*, 2012, and references therein). Thus, it appears that some 40 km of mantle lithosphere were converted to asthenosphere, similar to the lithosphere loss in the Kaapvaal craton that preceded intensive Cretaceous kimberlite magmatism (Kobussen *et al.*, 2008; Mather *et al.*, 2011). This is supported by textural evidence for recent mineralogical changes in the peridotite xenoliths studied here, as will be discussed below, and by a progressive shallowing of magma sources during breakup of the North Atlantic craton (Tappe *et al.*, 2008). If phlogopite addition at 90–110 km depth shortly prior to kimberlite magma emplacement at *c.* 150 Ma is responsible for generating the seismic discontinuity observed by Kumar *et al.* (2005), this indicates that, at least in the case of the SW-GNAC, the cratonic MLD is related to relatively young

metasomatism and is not a vestige of anisotropy generated during craton construction (see Rader *et al.*, 2015; Selway *et al.*, 2015; Aulbach *et al.*, 2017).

Garnet destabilization during Mesozoic rifting and lithosphere thinning

Mg# in cpx shows a marked anti-correlation with TiO_2 in our sample suite. The two most refractory samples (Mg# 93·5 and 93·6) have cpx with low Ti (≤ 320 ppm) and Yb contents ($\leq 0·16$ ppm). Such low concentrations cannot be attained by melt extraction from spinel peridotite without prior exhaustion of cpx, which occurs at 27% of peritectic melting of a fertile spinel peridotite with 620 ppm Ti and 0·5 ppm Y [modelling of McCoy-West *et al.* (2015)]. This apparent conflict may be reconciled if these garnet-free samples are not true spinel-facies peridotites, but rather peridotites that were originally in equilibrium with garnet. If the pressure–temperature calculations are accurate, all lherzolites and harzburgites and some phl-wehrlites and dunites recording pressures >3 GPa should be in the garnet stability field.

It is possible that garnet originally existed, at least in the higher-pressure lherzolites, but was destabilized as evidenced by symplectitic mineral assemblages (e.g. Godard & Martin, 2000) (Figs 2c and 3f). Relationships of Sc–Zr and Mn–Al in olivine have been suggested to be indicative of source lithology (De Hoog *et al.*, 2010). In more recent work (Bussweiler *et al.*, 2017), Al–V systematics have been used to distinguish the various facies and results indicate that the lherzolites are largely derived from the garnet stability field, whereas the wehrlites are derived from the garnet–spinel stability field (Supplementary Data Electronic Appendix 11).

The former presence of garnet in these symplectites may be reflected in low Al_2O_3, Y and HREE in the pyroxenes (owing to initial partitioning into garnet, followed by redistribution into symplectitic mineral assemblages after garnet). Indeed, lherzolitic opx has lower Al_2O_3 contents than that in the severely depleted garnet-free peridotites from the eastern GNAC and than in the vast majority of spinel peridotites from the Siberian craton (Ionov *et al.*, 2010; Doucet *et al.*, 2012), although somewhat higher Al_2O_3 than opx in Siberian garnet peridotites (Fig. 5c). It is also conspicuous that cpx in several lherzolites has very low MREE and HREE contents, more similar to that in Siberian garnet peridotites (Fig. 7). Moreover, spinels in the samples have Cr# ranging from 73 to 90 (Supplementary Data Electronic Appendix 4), which is typical for spinels coexisting with garnet (Ziberna *et al.*, 2013).

The geothermal gradient obtained for a suite of garnet peridotites at the same localities (Pyramidefjeld and Midternaes) is equivalent to an ~42–44 mW m^{-2} surface heat flow (Nielsen *et al.*, 2008), which is elevated relative to that of undisturbed cratonic lithosphere with gradients corresponding to ~35–40 mW m^{-2} surface heat flow (Grütter, 2009). A lower geothermal gradient (~38 mW m^{-2}) was obtained for mantle xenoliths from

the NW-GNAC, which were entrained during 590–550 Ma emplacement of kimberlites and ultramafic lamprophyres (Sand *et al.*, 2009). This suggests that substantial heating and related lithosphere thinning, related to incipient breakup of the NAC, occurred in the time interval up to the Jurassic kimberlite emplacement at *c.* 150 Ma in the southwestern part of the craton (Tappe *et al.*, 2007, 2009, 2012; Larsen *et al.*, 2009). These processes were probably accompanied by decompression owing to rifting, during which garnet was destabilized, as observed in Antarctica and the East African Rift (see Foley *et al.*, 2006; Kaeser *et al.*, 2006). The observation that cryptocrystalline and fine-grained mineral aggregates have persisted in pseudomorphs and that the pyroxene compositions still reflect the original presence of garnet suggests that garnet destabilization occurred only shortly prior to kimberlite magma eruption, with insufficient time for textural and compositional re-equilibration under upper mantle conditions.

Mineralogical and compositional changes during interaction with an evolving melt

The major and trace element relationships of the major silicate minerals in the mantle xenoliths under investigation reveal distinct composional and mineralogical differences between opx-bearing peridotites (lherzolites, harzburgites) and orthopyroxene-free peridotites (wehrlites, peridotites with inferred altered pyroxene), suggesting sampling of at least two distinct mantle regions with different metasomatic histories (Figs 4, 6 and 9). To aid in the identification of metasomatic agents, basaltic, silicocarbonatitic and carbonatitic melts in equilibrium with cpx were calculated using published distribution coefficients from Green *et al.* (2000), Girnis *et al.* (2013) and Dasgupta *et al.* (2009), respectively, and are compared with natural counterparts following the approach outlined by Aulbach *et al.* (2013).

Dunites, harzburgites and lherzolites: products of interaction with hydrous silicate melt

Lherzolitic cpx has an Mg# showing a marked anti-correlation with TiO_2, which could result either from melt depletion or from refertilization. The very low Mg#, in particular in the phlogopite-bearing variety, is inconsistent with melt extraction and rather suggests refertilization. Using Mg# as a proxy for the enrichment of lherzolites, it appears that FeO, Mn, TiO_2, and potentially Na_2O, V, Ga and Zn were added, whereas CaO and SiO_2 were diluted; Sr, Y, the REE or HFSE do not vary with Mg#. This may be due to additional cryptic metasomatic episodes, which disturbed the expected relationships between incompatible and major elements (Figs 4–6). The trend to very low Mg# in dunites indicates that these samples are pyroxene-free owing to reactive interaction with a silica-undersaturated melt and olivine crystallization (Pearson & Wittig, 2014) rather than owing to melt extraction, as also observed in the Kaapvaal cration (Rehfeldt *et al.*, 2008). The offset to
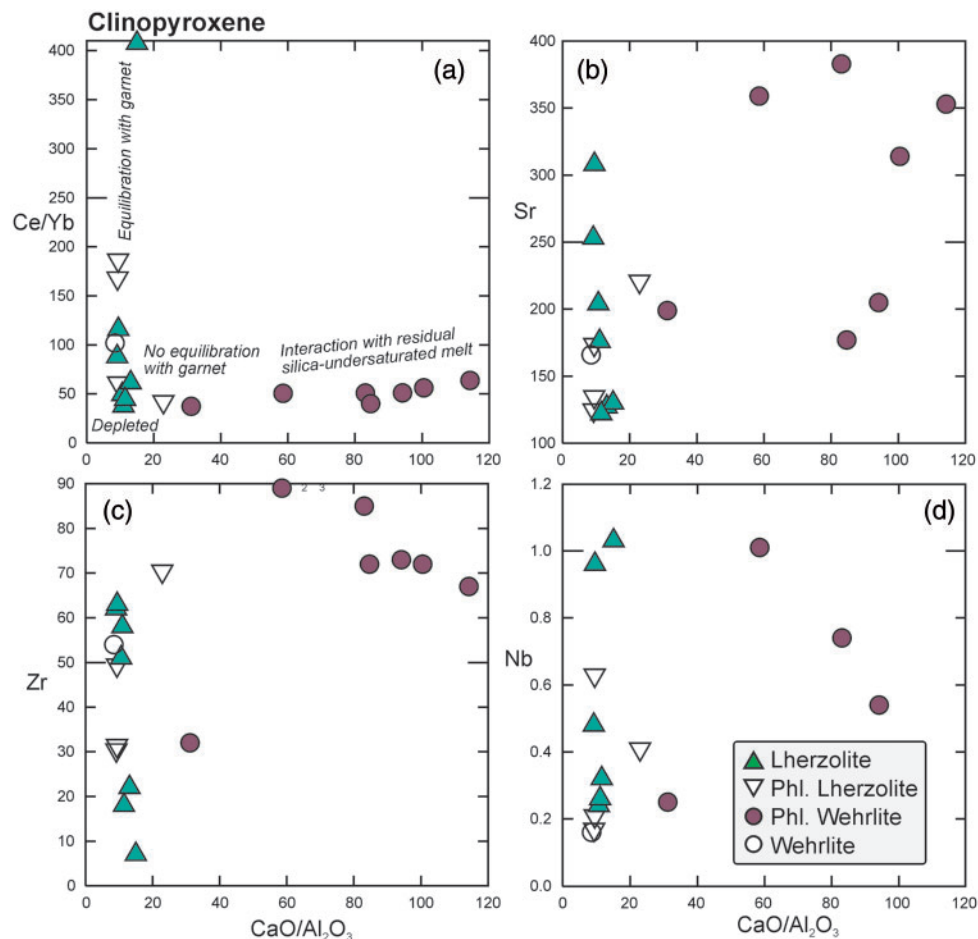
Fig. 9. Trace element abundances (ppm) and ratios in cpx as a function of CaO/Al_2O_3, illustrating the effect of metasomatism on wehrlitic cpx, which formed in originally highly depleted peridotite. Ce/Yb is a measure not only of metasomatic enrichment, but also of variable equilibration with garnet, where high Ce/Yb reflects metasomatism and/or equilibrium with garnet, whereas low Ce/Yb reflects depletion and/or cpx formed or added after garnet breakdown (see text for details).

lower Na, Al and Ca in olivine may reflect the attendant loss of pyroxenes, which no longer buffer the concentrations of these elements. In summary, the major and minor element relationshps in lherzolitic and dunitic olivine and opx (Figs 4 and 5) suggest metasomatism by silicate melts, which can efficiently mobilize TiO_2 (as opposed to carbonated melts or hydrous fluids; Coltorti *et al.*, 1999; Kessel *et al.*, 2005). The effects of this metasomatism include an increase in incompatible major and minor oxides (TiO_2, MnO, FeO) and dilution of compatible oxides (MgO, NiO) and are initially 'stealthy' (addition of cpx to a cpx-bearing assemblage), but are patent in the advanced stages (addition of phlogopite) (O'Reilly & Griffin, 2013).

Conspicuously, olivine in phlogopite-bearing varieties shows an offset to lower MnO at a given Mg# compared with phlogopite-free lherzolites, but has similar Na, P, Al and Ca contents. As the presence of phlogopite is reflected in the distinct compositions of olivine and the pyroxenes, these minerals are in compositional equilibrium in addition to textural equilibrium, and phlogopite therefore is not related to late addition from

kimberlite during transport to the surface. The distinct MnO at a given Mg# in olivine from phlogopite-bearing lherzolites and dunites argues against a continuum in metasomatic intensity from phlogopite-free to phlogopite-bearing varieties. Instead, it may reflect the distinct composition of the metasomatic agent.

As the median temperatures of last equilibration recorded for phlogopite-bearing lherzolites and harzburgites ($\sim$1000°C; Table 1) and for phlogopite-free lherzolites (1040°C) are fairly low, the most likely metasomatic agents would be hydrous fluids or volatile-rich melts, which are stable to lower temperatures during percolation of a peridotite matrix than volatile-poor melts (Dasgupta, 2013; Green *et al.*, 2014). Containing only $\sim$5 wt % FeO, natural carbonatites are not efficient media with which to explain the decreasing Mg# in olivine (8·6 wt % for lherzolites and 11·3 wt % for phlogopite lherzolites). We consider a small-volume, hydrous silicate melt the most likely metasomatic agent to explain the compositional relationships in the lherzolites (concomitant enrichment in FeO, MnO and TiO_2). In this case, the marked depletion in Y and the HREE in the

hypothetical basanite melts in equilibrium with cpx compared with natural basanites (Supplementary Data Electronic Appendix 12) may be an artefact of post-addition subsolidus re-equilibration of cpx with garnet (prior to its destabilization). If so, the concentrations of calculated melts in equilibrium with cpx will be inaccurate for the elements so affected. Inter-element fractionation could also result from percolative flow and associated chromatographic effects (Navon et al., 1996) rather than sub-solidus re-equilibration. It is not possible to constrain whether this melt had a sublithospheric origin or formed by partial melting of refertilized, deep lithospheric mantle. Variable contributions from phlogopite- and carbonate-bearing metasomes may explain the compositional differences between phlogopite-bearing and phlogopite-free lherzolites, harzburgites and dunites.

Wehrlites and pyroxene-free peridotites: products of interaction with strongly silica-undersaturated melt

Wehrlites represent a visibly metasomatized non-primitive peridotite assemblage that has been affected by opx loss and addition of phlogopite, cpx ± olivine and spinel by interaction with a silica-undersaturated melt (Kelemen et al., 1997; Shaw et al., 1998). Given that they occur at a shallower depth (90–110 km) than the lherzolites and harzburgites (100–170 km), they were probably initially more refractory. This is plausible given that larger melting intervals (to lower pressures) can be realized during cratonic lithosphere formation, and that highly depleted coarse harzburgites were entrained at similar depths in the NW-GNAC at 590–540 Ma (Sand et al., 2009).

Abundances of Ca in olivine are variable, but overall low, which may be due to equilibration at lower temperatures. Nevertheless, Ca-rich metasomatism may be reflected in high Ca/Al in wehrlitic olivine, accompanied by high MnO, Li, Zn, Mo, Cd and ln, and low P, Al and Cu (Fig. 4; Supplementary Data Electronic Appendix 13). Olivine in pyroxene-free peridotites, both phlogopite-bearing and phlogopite-free, has compositional characteristics very similar to olivine in wehrlites, suggesting interaction with a similar, or even the same, metasomatic agent. The observation that these samples contain patches with well-defined grain boundaries now filled with a cryptocrystalline alteration product (Fig. 3f) suggests that this metasomatism occurred relatively recently, after the last—presumably fluid- or melt-induced—recrystallization. They may represent a less advanced metasomatic product (post-alteration of pyroxenes, but prior to precipitation of secondary cpx and phlogopite) of the same metasomatic agent that affected the phl-wehrlites.

Wehrlitization has been ascribed to interaction with carbonated melts (Yaxley et al., 1991, 1998) or to reactive percolation of underplated silicate melts (Ionov et al., 2005) and was invoked to explain the source composition of nephelinites at 140 Ma in the Labradorian

part of the NAC mantle (Tappe et al., 2007). Yaxley et al. (1991) recognized increased CaO/Al$_2$O$_3$ and low TiO$_2$ in bulk-rocks, observed here in cpx along with LREE enrichment (Figs 6b and 9a), as the hallmarks of carbonatite metasomatism. Because the phl-wehrlites last equilibrated at lower temperatures than the lherzolites, the metasomatic agent must have been a volatile-rich, small-volume melt, as also suggested by the addition of phlogopite. Such melts are expected to form from peridotite in the presence of H$_2$O and CO$_2$ (Foley et al., 2009).

Both Mg-carbonatite and kimberlite have calculated H$_2$O contents (∼3·9 and 3·6 wt %, respectively; Tappe et al., 2017) that can explain the addition of phlogopite, but other compositional features of the phl-wehrlites are more difficult to explain by simple interaction with Mg-carbonatite or kimberlite. For example, median Sc concentrations in wehrlitic cpx are 176 ppm, higher than in natural carbonatites or kimberlites (13 ppm and 21 ppm, respectively, for Tikiusaaq), and higher than in lherzolitic cpx (31 ppm), or the basanites (25 ppm) that are inferred to have metasomatized the lherzolites, as discussed above. It is noteworthy that Sc is abundant in garnet, which may have been destabilized in the deeper opx-bearing lithologies during Mesozoic rifting, as discussed above. If the median pressure estimate for phl-wehrlites is accurate (3·0 GPa), they may be close to the garnet-out boundary, especially in depleted peridotite (Ziberna et al., 2013).

Element redistribution owing to melt-assisted garnet breakdown and during sulphide saturation

Several elements that are compatible in garnet, but less so in cpx (Sc, Y, In, Cd, Y; van Westrenen et al., 1999; Adam & Green, 2006; Mallmann & O'Neill, 2009; Davis et al., 2013) are noticeably enriched in wehrlitic cpx. Garnet breakdown in the deeper lithosphere owing to interaction with relatively hot hydrous silicate melts and partitioning into newly formed cpx in garnet-free peridotites at lower pressure may explain the higher concentrations of these elements in phl-wehrlites compared with lherzolites. This process may be gauged by Y concentrations in lherzolitic cpx, where low concentrations indicate equilibrium with garnet, whereas increasing concentrations would be due to cpx crystallization during and after garnet breakdown. The concentration of Y is not correlated with Mg# in cpx, suggesting that it is not exclusively controlled by melt depletion and refertilization. Instead, increasing concentrations of Sc, Zr, Cd, In and the HREE with Y are explained by liberation of these elements owing to garnet destabilization and their repartitioning into cpx (Fig. 10a–d).

In contrast to the sympathetic behaviour of Y, Sc, In and Cd, increasing Y concentrations in lherzolitic cpx are accompanied by a decrease in Co, Ni and Cu (Fig. 10e and f), which are the constituent metals in lithospheric base metal sulphides (Lorand et al., 2013). Sulphur may be carried as sulphate in oxidizing melts
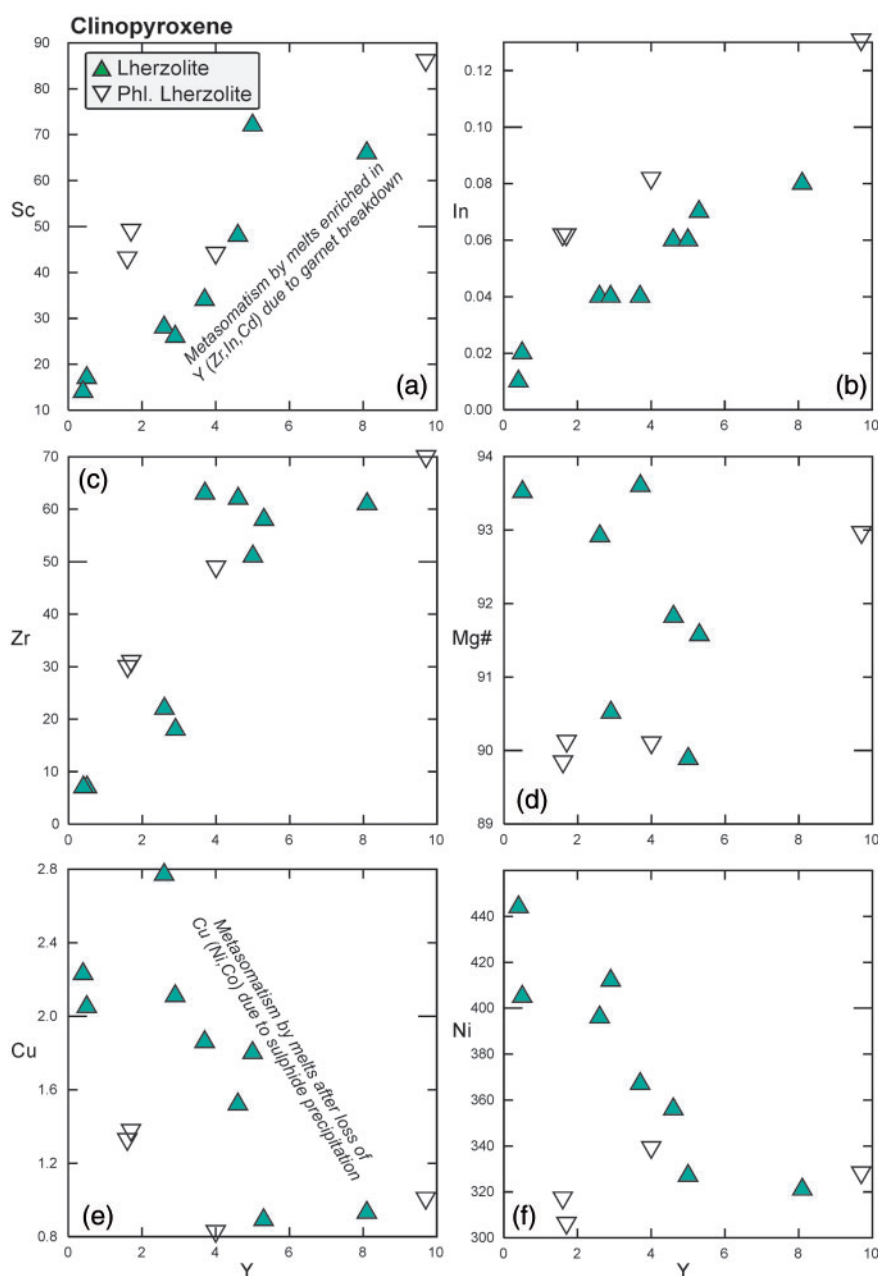
Fig. 10. Trace elements (ppm) and Mg# [100Mg/(Mg + Fe) molar] as a function of Y content in cpx; the latter is here taken as a proxy for progressive garnet-breakdown and repartitioning of garnet-compatible elements into coexisting cpx or newly precipitated cpx. Hf mimics the behaviour of Zr and Co mimics the behaviour of Ni (not shown). Concomitant sulphide saturation may be reflected in decreasing Co, Ni and Cu abundances.

and precipitated as sulphide along with metasomatic silicates (e.g. cpx) during melt–rock interactions at decreasing melt mass (Lorand *et al.*, 2013), leading to a depletion of Co, Ni and Cu. Therefore, it seems plausible that the metasomatic melts not only destabilized garnet and added cpx, but also introduced sulphides, which are abundant in the sample suite studied here. This agrees with the observation that the patently metasomatized phl-lherzolites have considerably lower median Cu contents than phlogopite-free lherzolites. Crystallization of secondary sulphide also occurred in peridotites from the NW-GNAC (Wittig *et al.*, 2008) and

in the Kaapvaal craton in the context of kimberlite-related hydrous melt metasomatism (Giuliani *et al.*, 2013).

V–Sc systematics of peridotite minerals: effects of redox, temperature and metasomatic enrichment

The redox sensitivity of V has led to its use as a proxy for oxygen fugacity during mantle melting (Canil 1997, 2002; Mallmann & O'Neill, 2009). Redox effects on V are, however, compounded by the temperature dependence of its partitioning into olivine (Witt-Eickschen &

O'Neill, 2005; De Hoog et al., 2010). The ratio of V to a geochemically similar homovalent element, such as Sc, has been used to eliminate the effects of the degree of partial melt extraction or fractional crystallization (Lee et al., 2005), and this may also to a first approximation apply to temperature effects. Bulk V/Sc in the residue would be expected to increase during progressive melt extraction under reducing conditions when V behaves less incompatibly [–2 relative to the fayalite–magnetite–quartz oxygen buffer (FMQ); Lee et al., 2005]. Such low f_{O_2} values are typically encountered in cratonic peridotites (Foley, 2011). Indeed, pre-metasomatic olivine grains in xenoliths from the Kaapvaal and Slave cratons have higher V/Sc than metasomatized ones (Foley et al., 2013).

Owing to the strong compatibility of Sc in garnet (e.g. Davis et al., 2013), this mineral has low V/Sc (e.g. in Siberian garnet peridotites: median of 1·8; Howarth et al., 2014) compared with bulk primitive mantle with a ratio of 4·9 (values of McDonough & Sun, 1995). Thus, progressive garnet breakdown and redistribution into cpx might explain the strong correlation of V/Sc with Sc, which is not evident for V (Supplementary Data Electronic Appendix 14). This complicates interpretation of V–Sc systematics in cpx in terms of redox effects. In addition, it has been shown that cpx–melt distribution coefficients for V vary several orders of magnitude less than in olivine as a function of f_{O_2} (Mallmann & O'Neill, 2009). Thus, we focus here on the V–Sc systematics of olivine to make inferences on redox conditions during the metasomatic enrichment of the lithosphere beneath the SW-GNAC.

In the opx-bearing assemblages and dunites, both V and Sc in olivine show an anti-correlation with Mg# as a proxy for degree of melt depletion and refertilization (Fig. 11), but V/Sc does not covary with Mg#, and V and Sc are not correlated with each other. It is notable that in olivine from lherzolites and phl-lherzolites V concentrations vary more strongly (4·2-fold) than Sc concentrations (1·4-fold). The four samples with the highest V (5·5–9 ppm) and V/Sc (6·7–7·7) are markedly offset towards high Cu contents (Supplementary Data Electronic Appendix 13), suggesting lack of equilibrium with sulphide, which crystallized during an advanced stage of metasomatism (see the previous section). The distinctly high V/Sc of olivine in the three lherzolites with Mg# >91, which is similar to that of olivine from some Kaapvaal and Slave peridotites (Foley et al., 2013), is thus interpreted as reflecting original melt depletion under reducing conditions when V is less incompatible in olivine (Mallmann & O'Neill, 2009). Because the lithospheric mantle becomes more reducing with depth (Woodland & Koch, 2003; Foley, 2011), high V and V/Sc in these lherzolites may reflect a combination of higher pressure of equilibration (hence more reducing conditions) and little interaction with oxidizing melts during mantle metasomatism (Woodland et al., 1996; Yaxley et al., 2012). Apparently increased partitioning of V into olivine at high temperature (De Hoog et al., 2010), as

suggested by the weak positive correlation of V and V/Sc with iterative T_{Al-ol} (Fig. 11), may thus reflect more reducing conditions along a cratonic geotherm rather than increased partitioning of V into olivine at high temperatures. Olivine in some phl-lherzolites with lower Mg# has similarly high V concentrations (5·4–6 ppm) but higher Sc concentrations, translating into lower V/Sc (3·6–4·3) for these samples. This combination possibly indicates metasomatism under reducing conditions. Olivine in the remaining lherzolites and in dunites has both lower V and higher Sc concentrations, hence lower V/Sc, which may reflect more oxidative metasomatism (Fig. 11).

The low V and V/Sc of olivine in phl-wehrlites and in pyroxene-free peridotites are similar to those reported for strongly metasomatized peridotites from the Kaapvaal craton (Foley et al., 2013). It is plausible that the metasomatic melt became more oxidizing as it percolated upwards owing to sulphide precipitation (as inferred from low Cu contents, discussed above), and preferred incorporation of Fe^{2+} into precipitating and reacting minerals, whereas Fe^{3+} is more incompatible (Canil et al., 1994). Because carbonates were not deposited, any CO_2 component carried by the melt would have been relatively concentrated, further increasing the oxidizing potential of the melt. Under such oxidizing conditions, V would be expected to be more incompatible (Mallmann & O'Neill, 2009), explaining low concentrations in wehrlitic minerals, although a temperature effect cannot be firmly excluded. These considerations illustrate that a straightforward interpretation of olivine V–Sc systematics is complicated and caution is required when using them as redox proxies.

Timing of metasomatism, and relationship to alkaline ultramafic melts in cratonic Greenland

Chemical and mineralogical evidence suggests that lherzolites and harzburgites residing at greater depths (median ~140 km) and opx-free wehrlites residing at shallower depths (~100 km) reflect quasi-contemporaneous metasomatism by a melt that originated as a hydrous silicate melt and became progressively more silica-undersaturated by precipitation of cpx and attendant garnet breakdown. Upward percolation of this melt, which was enriched in highly incompatible elements and those that are typically abundant in garnet, into shallower portions of the lithosphere led to opx dissolution, precipitation of cpx and phlogopite, and incompatible element enrichment. The compositional gap between opx-bearing peridotites and phl-wehrlites, which is accompanied by a difference in temperatures and hence position in the lithosphere column, may reflect a change in melt migration style imposed by temperature and rheology (McKenzie, 1989; Sleep, 2009).

There is textural and mineralogical evidence for the former presence of garnet in some lherzolites and for the former presence of pyroxenes in some peridotites that are otherwise similar to the phl-wehrlites, indicating that recrystallization has not occurred in these rocks
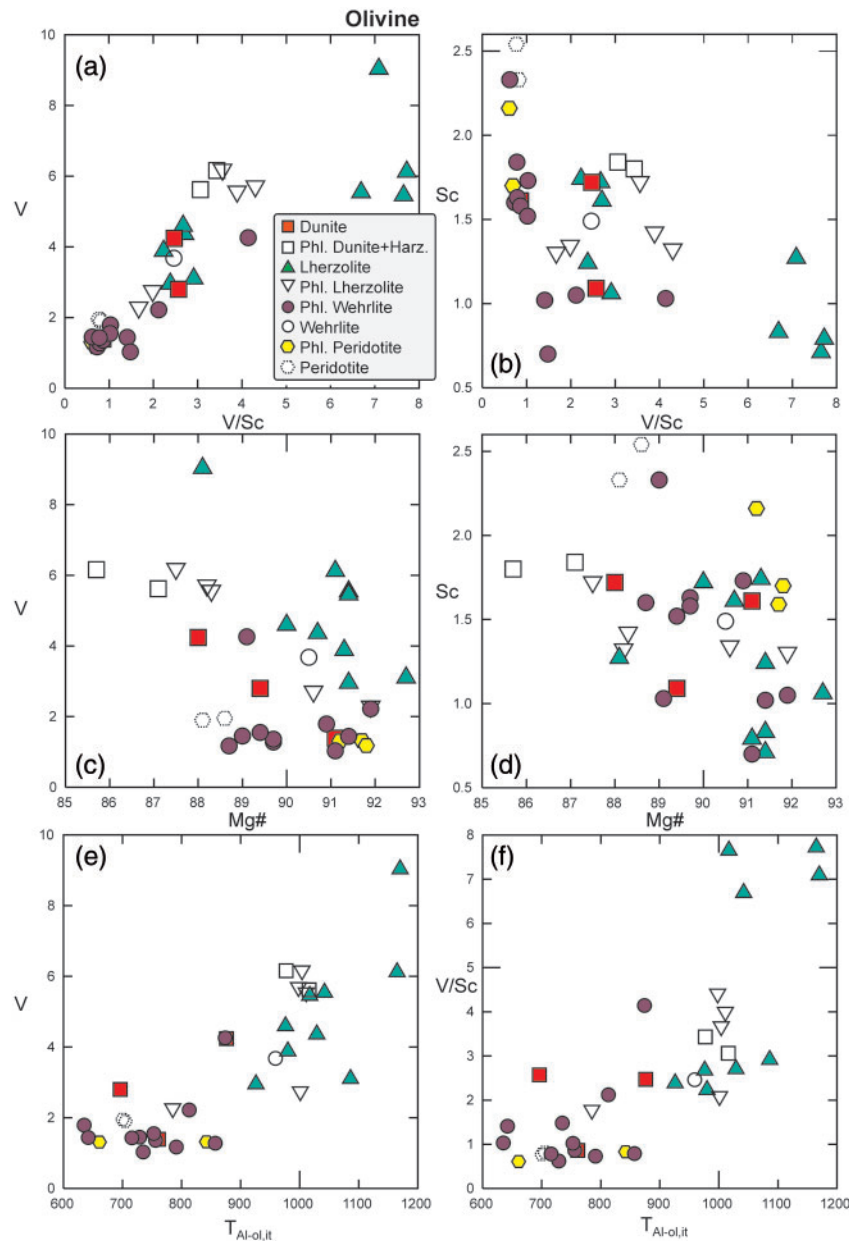
Fig. 11. V–Sc–Mg# relationships in olivine (a–d), and V (e) and V/Sc (f) as a function of iteratively calculated T_{Al-ol} ($T_{Al-ol, it}$).

since garnet breakdown. In contrast, the apparent compositional and textural equilibrium between olivine and newly introduced cpx suggests qualitatively that the timing of this event was long enough ago to allow compositional equilibration. Relatively homogeneous Sr–Sm–Nd isotopic compositions of cpx separates from a wehrlite and three lherzolites suggest efficient isotopic homogenization.

Whereas the average initial (at ~150 Ma) $^{143}Nd/^{144}Nd$ for cpx of 0·51270 ($\varepsilon_{Nd,i}$ +5·1) is identical to that obtained for the nearby *c.* 160 Ma Tikiusaaq kimberlite dykes (0·51268), the inital $^{87}Sr/^{86}Sr$ of 0·70375 is distinctly higher than in the kimberlite (0·70334; Tappe *et al.*, 2012). This suggests that the mantle lithosphere beneath the SW-GNAC interacted with a metasomatic

agent that was isotopically similar but not identical to the host kimberlite. This possibly occurred during an event precursory to kimberlite magmatism and involved a melt leaving an isotopically slightly more evolved source (at higher Rb/Sr), perhaps reflecting a small contribution from phlogopite-bearing assemblages ('metasomes'; Tappe *et al.*, 2007, 2008) to the melt, as was argued for the Neoproterozoic Sarfartoq kimberlites straddling the northern GNAC boundary (Tappe *et al.*, 2011*a*, 2012).

Mesozoic kimberlites with very homogeneous isotopic compositions have been suggested to reflect little contribution from phlogopite-rich metasomes, which had been consumed during earlier ultramafic melt magmatism (Tappe *et al.*, 2011*a*, 2012). The predominance

of modally metasomatized cpx–phlogopite-bearing peridotite xenoliths in this study is not inconsistent with this suggestion, as they occur at relatively shallow levels, above the depth of kimberlite melt generation ($>$150 km), which is constrained by the presence of diamond and mantle xenoliths with higher equilibration pressures (Wittig *et al.*, 2008, 2010; Sand *et al.*, 2009; Tappe *et al.*, 2011*b*, 2012). Therefore, the metasomatized mantle xenoliths investigated here are interpreted not as sources but as expressions of deep magmatism beneath the SW-GNAC that was precursory to Mesozoic kimberlite emplacement. This is plausible because small-volume melts will initially partially or completely crystallize in the cooler and more viscous cores of the shallow cratonic mantle lithosphere (McKenzie, 1989; Sleep, 2009). The enrichment involves zones around magmatic conduits that can extend to higher levels whereas most of the cratonic lithosphere remains un-enriched at the same depths (Griffin *et al.*, 2013). This mantle keel 'conditioning', together with extensional stresses that act during the beginning of continental breakup, may have been instrumental in paving the way for successful subsequent extraction of kimberlite magmas (Wyllie, 1980; Giuliani *et al.*, 2014; Tappe *et al.*, 2017).

SUMMARY AND CONCLUSIONS

We applied a detailed petrographic and *in situ* analytical approach to a new suite of fresh kimberlite-borne peridotite xenoliths ($n = 42$) from the Pyramidefjeld and Midternaes kimberlite sheets in cratonic SW Greenland to unravel the evolution of the underlying mantle lithosphere in the context of available geochemical, geophysical and dynamic constraints. Our main conclusions are as follows.

1. The mantle beneath Pyramidefjeld and Midternaes is stratified, with lherzolites, harzburgites and dunites residing at ~100–170 km depth. The former presence of garnet is indicated by pyroxene–spinel assemblages occupying former coarse grains. In contrast, phlogopite-bearing, texturally equilibrated wehrlites, which show evidence for recent pyroxene breakdown, occur at ~90–110 km depth. This overlaps with negative seismic velocity gradients that have been interpreted as a mid-lithospheric discontinuity beneath western Greenland.

2. Metasomatism by a hydrous silicate melt precursory to *c.* 150 Ma kimberlite eruption is inferred from continuous trends in the lherzolites, harzburgites and dunites towards lower mineral Mg# at increasing TiO_2, MnO and Na_2O and decreasing NiO contents. Elements released during garnet breakdown (Y, Sc, In and the HREE) were redistributed into newly formed clinopyroxene, whereas depletions in Cu, Ni and Co are ascribed to concomitant sulphide saturation. These reactions led to evolution of the metasomatic melt towards a more silica-undersaturated and oxidizing composition at decreasing melt volume.

3. The residual melt percolated upwards and metasomatized the shallower lithosphere, with deposition of phlogopite and formation of cpx at the expense of opx. Cryptic effects are manifested in olivine with higher MnO at a given Mg#, higher Ca/Al, Li, Sc, Mo and In abundances, but lower Cu, Ti, Na, P, Al and V contents compared with olivine in the deeper lherzolites. Low Al and V in part reflect lower equilibration temperatures, which is evident in lower $^{\text{clinopyroxene/olivine}}D$ for incompatible elements in wehrlites compared with lherzolites, whereas low V may additionally reflect higher incompatibility during oxidative metasomatism.

4. We suggest that the small-volume volatile-rich melt metasomatism conditioned the lithosphere for the emplacement of Mesozoic alkaline ultramafic melts across the North Atlantic craton. This was accompanied by the loss of some 40 km of lithospheric mantle and is recorded in the progressive shallowing of magma sources during the breakup of the North Atlantic craton.

SUPPLEMENTARY DATA

Supplementary data for this paper are available at *Journal of Petrology* online.

REFERENCES

Adam, J. & Green, T. (2006). Trace element partitioning between mica- and amphibole-bearing garnet lherzolite and hydrous basanitic melt: 1. Experimental results and the

investigation of controls on partitioning behaviour. *Contributions to Mineralogy and Petrology* **152**, 1–17.

Andrews, J. R. & Emeleus, C. H. (1975). Structural aspects of kimberlite dyke intrusion in southwest Greenland. *Physics and Chemistry of the Earth* **9**, 43–50.

Arndt, N. T. & Nisbet, E. G. (2012). Processes on the young Earth and the habitats of early life. *Annual Review of Earth and Planetary Sciences* **40**, 521–549.

Aulbach, S. (2012). Craton nucleation and formation of thick lithospheric roots. *Lithos* **149**, 16–30.

Aulbach, S. & Viljoen, K. S. (2015). Eclogite xenoliths from the Lace kimberlite, Kaapvaal craton: from convecting mantle source to palaeo-ocean floor and back. *Earth and Planetary Science Letters* **431**, 274–286.

Aulbach, S., Griffin, W. L., Pearson, N. J. & O'Reilly, S. Y. (2013). Nature and timing of metasomatism in the stratified mantle lithosphere beneath the Central Slave craton (Canada). *Chemical Geology* **352**, 153–169.

Aulbach, S., Massuyeau, M. & Gaillard, F. (2017). Origins of cratonic mantle discontinuities: a view from petrology, geochemistry and thermodynamic models. Invited review article. *Lithos* **268–271**, 364–382.

Bennett, V. C., Brandon, A. D. & Nutman, A. P. (2007). Coupled ^{142}Nd–^{143}Nd isotopic evidence for Hadean mantle dynamics. *Science* **318**, 1907–1910.

Bernstein, S., Kelemen, P. B. & Brooks, C. K. (1998). Depleted spinel harzburgite xenoliths in Tertiary dykes from east Greenland: restites from high degree melting. *Earth and Planetary Science Letters* **154**, 221–235.

Bernstein, S., Hanghøj, K., Kelemen, P. B. & Brooks, C. K. (2006). Ultra-depleted, shallow cratonic mantle beneath West Greenland: dunitic xenoliths from Ubekendt Ejland. *Contributions to Mineralogy and Petrology* **152**, 335–347.

Bernstein, S., Szilas, K. & Kelemen, P. B. (2013). Highly depleted cratonic mantle in West Greenland extending into diamond stability field in the Proterozoic. *Lithos* **168**, 160–172.

Bizzarro, M. & Stevenson, R. K. (2003). Major element composition of the lithospheric mantle under the North Atlantic craton: evidence from peridotite xenoliths of the Sarfartoq area, southwestern Greenland. *Contributions to Mineralogy and Petrology* **146**, 223–240.

Blichert-Toft, J. & Puchtel, I. S. (2010). Depleted mantle sources through time: evidence from Lu–Hf and Sm–Nd isotope systematics of Archean komatiites. *Earth and Planetary Science Letters* **297**, 598–606.

Bussweiler, Y., Brey, G. P., Pearson, D. G., Stachel, T., Stern, R. A., Hardman, M. F., Kjarsgaard, B. A. & Jackson, S. E. (2017). The aluminum-in-olivine thermometer for mantle peridotites - Experimental versus empirical calibration and potential applications. *Lithos* **272**, 301–314.

Canil, D. (1997). Vanadium partitioning and the oxidation state of Archaean komatiite magmas. *Nature* **389**, 842–845.

Canil, D. (2002). Vanadium in peridotites, mantle redox and tectonic environments: Archean to present. *Earth and Planetary Science Letters* **195**, 75–90.

Canil, D., O'Neill, H. S., Pearson, D. G., Rudnick, R. L., McDonough, W. F. & Carswell, D. A. (1994). Ferric iron in peridotites and mantle oxidation states. *Earth and Planetary Science Letters* **123**, 205–220.

Cherniak, D. J. & Liang, Y. (2012). Ti diffusion in natural pyroxene. *Geochimica et Cosmochimica Acta* **98**, 31–47.

Coltorti, M., Bonadiman, C., Hinton, R. W., Siena, F. & Upton, B. G. J. (1999). Carbonatite metasomatism of the oceanic upper mantle: evidence from clinopyroxenes and glasses in ultramafic xenoliths of Grande Comore, Indian Ocean. *Journal of Petrology* **40**, 133–165.

Dasgupta, R. (2013). Ingassing, storage, and outgassing of terrestrial carbon through geologic time. In: Hazen, R. M., Jones, A. P. and Baross, J. A. (eds) Carbon in Earth. *Mineralogical Society of America and Geochemical Society, Reviews in Mineralogy and Geochemistry* **75**, 183–229.

Dasgupta, R., Hirschmann, M. M., McDonough, W. F., Spiegelman, M. & Withers, A. C. (2009). Trace element partitioning between garnet lherzolite and carbonatite at 6·6 and 8·6 GPa with applications to the geochemistry of the mantle and of mantle-derived melts. *Chemical Geology* **262**, 57–77.

Davis, F. A., Humayun, M., Hirschmann, M. M. & Cooper, R. S. (2013). Experimentally determined mineral/melt partitioning of first-row transition elements (FRTE) during partial melting of peridotite at 3 GPa. *Geochimica Et Cosmochimica Acta* **104**, 232–260.

De Hoog, J. C. M., Gall, L. & Cornell, D. H. (2010). Trace-element geochemistry of mantle olivine and application to mantle petrogenesis and geothermobarometry. *Chemical Geology* **270**, 196–215.

Doucet, L. S., Ionov, D. A., Golovin, A. V. & Pokhilenko, N. P. (2012). Depth, degrees and tectonic settings of mantle melting during craton formation: inferences from major and trace element compositions of spinel harzburgite xenoliths from the Udachnaya kimberlite, Central Siberia. *Earth and Planetary Science Letters* **359–360**, 206–218.

Droop, G. T. R. (1987). A general equation for estimating Fe^{3+} concentrations in ferromagnesian silicates and oxides from microprobe analyses, using stoichiometric criteria. *Mineralogical Magazine* **51**, 431–435.

Eccles, D. R., Heaman, L. M., Luth, R. W. & Creaser, R. A. (2004). Petrogenesis of the late Cretaceous Northern Alberta kimberlite province. *Lithos* **76**, 435–459.

Eggins, S. M., Kinsley, L. P. J. & Shelley, J. M. G. (1998). Deposition and element fractionation processes during atmospheric pressure laser sampling for analysis by ICP-MS. *Applied Surface Science* **127**, 278–286.

Emeleus, C. H. & Andrews, J. R. (1975). Mineralogy and petrology of kimberlite dyke and sheet intrusions and included peridotite xenoliths from South-west Greenland. *Physics and Chemistry of the Earth* **9**, 179–198.

Foley, S. F. (2011). A reappraisal of redox melting in the Earth's mantle as a function of tectonic setting and time. *Journal of Petrology* **52**, 1363–1391.

Foley, S. F., Andronikov, A. V., Jacob, D. E. & Melzer, S. (2006). Evidence from Antarctic mantle peridotite xenoliths for changes in mineralogy, geochemistry and geothermal gradients beneath a developing rift. *Geochimica et Cosmochimica Acta* **70**, 3096–3120.

Foley, S. F., Yaxley, G. M., Rosenthal, A., Buhre, S., Kiseeva, E. S., Rapp, R. P. & Jacob, D. E. (2009). The composition of near-solidus melts of peridotite in the presence of CO_2 and H_2O between 40 and 60 kbar. *Lithos* **112**, 274–283.

Foley, S. F., Prelevic, D., Rehfeldt, T. & Jacob, D. E. (2013). Minor and trace elements in olivines as probes into early igneous and mantle melting processes. *Earth and Planetary Science Letters* **363**, 181–191.

Frei, D., Hutchison, M. T., Gerdes, A. & Heaman, L. M. (2008). Common-lead corrected U–Pb age dating of perovskite by laser ablation–magnetic sectorfield ICP-MS. *9th International Kimberlite Conference*, Frankfurt am Main, Germany, 9IKC-A-00216. Extended abstract.

Girnis, A. V., Bulatov, V. K., Brey, G. P., Gerdes, A. & Hoefer, H. E. (2013). Trace element partitioning between mantle minerals and silico-carbonate melts at 6–12 GPa and applications to mantle metasomatism and kimberlite genesis. *Lithos* **160**, 183–200.

Giuliani, A., Kamenetsky, V. S., Kendrick, M. A., Phillips, D., Wyatt, B. A. & Maas, R. (2013). Oxide, sulphide and carbonate minerals in a mantle polymict breccia: metasomatism by proto-kimberlite magmas, and relationship to the kimberlite megacrystic suite. *Chemical Geology* **353**, 4–18.

Giuliani, A., Phillips, D., Kamenetsky, V. S., Kendrick, M. A., Wyatt, B. A., Goemann, K. & Hutchinson, G. (2014). Petrogenesis of mantle polymict breccias: insights into mantle processes coeval with kimberlite magmatism. *Journal of Petrology* **55**, 831–858.

Glaser, S. M., Foley, S. F. & Günther, D. (1999). Trace element compositions of minerals in garnet and spinel peridotite xenoliths from the Vitim volcanic field, Transbaikalia, Eastern Siberia. *Lithos* **48**, 263–285.

Godard, G. & Martin, S. (2000). Petrogenesis of kelyphites in garnet peridotites: a case study from the Ulten zone, Italian Alps. *Journal of Geodynamics* **30**, 117–145.

Green, D. H., Hibberson, W. O., Rosenthal, A., Kovacs, I., Yaxley, G. M., Falloon, T. J. & Brink, F. (2014). Experimental study of the influence of water on melting and phase assemblages in the upper mantle. *Journal of Petrology* **55**, 2067–2096.

Green, T. H., Blundy, J. D., Adam, J. & Yaxley, G. M. (2000). SIMS determination of trace element partition coefficients between garnet, clinopyroxene and hydrous basaltic liquids at 2–7·5 GPa and 1080–1200 C. *Lithos* **53**, 165–187.

Griffin, W. L., O'Reilly, S. Y., Doyle, B. J., Pearson, N. J., Coopersmith, H., Kivi, K., Malkovets, V. & Pokhilenko, N. (2004). Lithosphere mapping beneath the North American plate. *Lithos* **77**, 873–922.

Griffin, W. L., Powell, W. J., Pearson, N. J. & O'Reilly, S. Y. (2008). A2. GLITTER: Data reduction software for laser ablation ICP–MS. In: Sylvester, P. (ed.) *Laser Ablation-ICPMS in the Earth Sciences: Current Practices and Outstanding Issues*. Vancouver BC: Mineralogical Association of Canada, p. 356.

Griffin, W. L., O'Reilly, S. Y., Afonso, J. C. & Begg, G. C. (2009). The composition and evolution of lithospheric mantle: a re-evaluation and its tectonic implications. *Journal of Petrology* **50**, 1185–1204.

Griffin, W. L., Begg, G. C. & O'Reilly, S. Y. (2013). Continental-root control on the genesis of magmatic ore deposits. *Nature Geoscience* **6**, 905–910.

Grütter, H. S. (2009). Pyroxene xenocryst geotherms: techniques and application. *Lithos* **112**, 1167–1178.

Hamilton, P. J., O'Nions, R. K., Bridgwater, D. & Nutman, A. (1983). Sm–Nd studies of Archean metasediments and metavolcanics from West Greenland and their implications for the Earth's early history. *Earth and Planetary Science Letters* **62**, 263–272.

Hanghøj, K., Kelemen, P., Bernstein, S., Blusztajn, J. & Frei, R. (2001). Osmium isotopes in the Wiedemann Fjord mantle xenoliths: a unique record of cratonic mantle formation by melt depletion in the Archaean. *Geochemistry, Geophysics, Geosystems* **2**, 2000GC000085.

Hoffman, P. F. (1989). Precambrian geology and tectonic history of North America. In: Bally, A. W. & Palmer, A. R. (eds) *The Geology of North America—An Overview*. Geological Society of America, pp. 447–512.

Howarth, G. H., Michael, E., Skinner, W. & Prevec, S. A. (2011). Petrology of the hypabyssal kimberlite of the Kroonstad group II kimberlite (orangeite) cluster, South Africa: evolution of the magma within the cluster. *Lithos* **125**, 795–808.

Howarth, G. H., Barry, P. H., Pernet-Fisher, J. F., Baziotis, I. P., Pokhilenko, N. P., Pokhilenko, L. N., Bodnar, R. J., Taylor, L. A. & Agashev, A. M. (2014). Superplume metasomatism: evidence from Siberian mantle xenoliths. *Lithos* **184**, 209–224.

Hutchison, M. T. & Heaman, L. M. (2008). Chemical and physical characteristics of diamond crystals from Garnet Lake, Sarfartoq, West Greenland: an association with carbonatitic magmatism. *Canadian Mineralogist* **46**, 1063–1078.

Hutchison, M. T., Nielsen, L. J. & Bernstein, S. (2007). *P–T* history of kimberlite-hosted garnet lherzolites from South-West Greenland. *Geological Survey of Denmark and Greenland Bulletin* **13**, 45–48.

Ionov, D. A., Chanefo, I. & Bodinier, J. L. (2005). Origin of Fe-rich lherzolites and wehrlites from Tok, SE Siberia by reactive melt percolation in refractory mantle peridotites. *Contributions to Mineralogy and Petrology* **150**, 335–353.

Ionov, D. A., Chazot, G., Chauvel, C., Merlet, C. & Bodinier, J. L. (2006). Trace element distribution in peridotite xenoliths from Tok, SE Siberian craton: a record of pervasive, multi-stage metasomatism in shallow refractory mantle. *Geochimica et Cosmochimica Acta* **70**, 1231–1260.

Ionov, D. A., Doucet, L. S. & Ashchepkov, I. V. (2010). Composition of the Lithospheric Mantle in the Siberian Craton: New Constraints from Fresh Peridotites in the Udachnaya-East Kimberlite. *Journal of Petrology* **51**, 2177–2210.

Jochum, K. P., Nohl, L., Herwig, K., Lammel, E., Toll, B. & Hofmann, A. W. (2005). GeoReM: A new geochemical database for reference materials and isotopic standards. *Geostandards and Geoanalytical Research* **29**, 333–338.

Kaeser, B., Kalt, A. & Pettke, T. (2006). Evolution of the lithospheric mantle beneath the Marsabit volcanic field (Northern Kenya): constraints from textural, *P–T* and geochemical studies on xenoliths. *Journal of Petrology* **47**, 2149–2184.

Kelemen, P. B., Hirth, G., Shimizu, N., Spiegelman, M. & Dick, H. J. B. (1997). A review of melt migration processes in the adiabatically upwelling mantle beneath oceanic spreading ridges. *Philosophical Transactions of the Royal Society, Series A* **355**, 283–318.

Kessel, R., Schmidt, M. W., Ulmer, P. & Pettke, T. (2005). Trace element signature of subduction-zone fluids, melts and supercritical liquids at 120–180 km depth. *Nature* **437**, 724–727.

Kjarsgaard, B. A., Pearson, D. G., Tappe, S., Nowell, G. M. & Dowall, D. P. (2009). Geochemistry of hypabyssal kimberlites from Lac de Gras, Canada: comparisons to a global database and applications to the parent magma problem. *Lithos* **112**, 236–248.

Kobussen, A. F., Griffin, W. L., O'Reilly, S. Y. & Shee, S. R. (2008). Ghosts of lithospheres past: imaging an evolving lithospheric mantle in Southern Africa. *Geology* **36**, 515–518.

Kumar, P., Kind, R., Hanka, W., Wylegalla, K., Reigber, C., Yuan, X., Woelbern, I., Schwintzer, P., Fleming, K., Dahl-Jensen, T., Larsen, T. B., Schweitzer, J., Priestley, K., Gudmundsson, O. & Wolf, D. (2005). The lithosphere–asthenosphere boundary in the North-West Atlantic region. *Earth and Planetary Science Letters* **236**, 249–257.

Larsen, L. M., Heaman, L. M., Creaser, R. A., Duncan, R. A., Frei, R. & Hutchison, M. (2009). Tectonomagmatic events during stretching and basin formation in the Labrador Sea and the Davis Strait: evidence from age and composition of Mesozoic to Palaeogene dyke swarms in West Greenland. *Journal of the Geological Society, London* **166**, 999–1012.

Lazarov, M., Woodland, A. B. & Brey, G. P. (2009). Thermal state and redox conditions of the Kaapvaal mantle: a study of xenoliths from the Finsch mine, South Africa. *Lithos* **112**, 913–923.

Lee, C. T. A., Leeman, W. P., Canil, D. & Li, Z. X. A. (2005). Similar V/Sc systematics in MORB and arc basalts:

implications for the oxygen fugacities of their mantle source regions. *Journal of Petrology* **46**, 2313–2336.

Lorand, J. P., Luguet, A. & Alard, O. (2013). Platinum-group element systematics and petrogenetic processing of the continental upper mantle: a review. *Lithos* **164–167**, 2–21.

Luchs, T., Brey, G. P., Gerdes, A. & Höfer, H. E. (2013). The lithospheric mantle underneath the Gibeon Kimberlite field (Namibia): a mix of old and young components—evidence from Lu–Hf and Sm–Nd isotope systematics. *Precambrian Research* **231**, 263–276.

Lugmair, G. W. & Marti, K. (1978). Lunar initial ^{143}Nd–^{144}Nd—differential evolution of lunar crust and mantle. *Earth and Planetary Science Letters* **39**, 349–357.

Mallmann, G. & O'Neill, H. S. C. (2009). The crystal/melt partitioning of V during mantle melting as a function of oxygen fugacity compared with some other elements (Al, P, Ca, Sc, Ti, Cr, Fe, Ga, Y, Zr and Nb). *Journal of Petrology* **50**, 1765–1794.

Mather, K. A., Pearson, D. G., McKenzie, D., Kjarsgaard, B. A. & Priestley, K. (2011). Constraints on the depth and thermal history of cratonic lithosphere from peridotite xenoliths, xenocrysts and seismology. *Lithos* **125**, 729–742.

McCoy-West, A. J., Bennett, V. C., O'Neill, H. S., Hermann, J. & Puchtel, I. S. (2015). The interplay between melting, refertilization and carbonatite metasomatism in off-cratonic lithospheric mantle under Zealandia: an integrated major, trace and platinum group element study. *Journal of Petrology* **56**, 563–604.

McDonough, W. F. & Sun, S. S. (1995). The composition of the Earth. *Chemical Geology* **120**, 223–253.

McKenzie, D. (1989). Some remarks on the movement of small melt fractions in the mantle. *Earth and Planetary Science Letters* **95**, 53–72.

Minster, J. F. & Allègre, C. J. (1980). More data on ^{87}Rb–^{87}Sr dating of LL chondrites. *Meteoritics* **15**, 333.

Navon, O., Frey, F. A. & Takazawa, E. (1996). Magma transport and metasomatism in the mantle: A critical review of current geochemical models - Discussion. *American Mineralogist* **81**, 754–759.

Nielsen, L. J., Hutchison, M. T. & Malarkey, J. (2008). Geothermal constraints from kimberlite-hosted garnet lherzolites from southern Greenland. *9th International Kimberlite Conference*. Frankfurt, Germany, 9IKC-A-00047. Extended abstract.

Nimis, P. & Grütter, H. (2010). Internally consistent geothermometers for garnet peridotites and pyroxenites. *Contributions to Mineralogy and Petrology* **159**, 411–427.

Nutman, A. P. & Friend, C. R. L. (2009). New 1:20,000 scale geological maps, synthesis and history of investigation of the Isua supracrustal belt and adjacent orthogneisses, Southern West Greenland: a glimpse of Eoarchaean crust formation and orogeny. *Precambrian Research* **172**, 189–211.

Nutman, A. P., Friend, C. R. L., Barker, S. L. L. & McGregor, V. R. (2004). Inventory and assessment of Palaeoarchaean gneiss terrains and detrital zircons in Southern West Greenland. *Precambrian Research* **135**, 281–314.

O'Reilly, S. Y., Chen, D., Griffin, W. L. & Ryan, C. G. (1997). Minor elements in olivine from spinel lherzolite xenoliths: implications for thermobarometry. *Mineralogical Magazine* **61**, 257–269.

O'Reilly, S. Y. & Griffin, W. L. (2013). Mantle metasomatism. In: Harlov, D. E. & Austrheim, H. (eds) *Metasomatism and the Chemical Transformation of Rock*. Springer, pp. 471–533.

Pearson, D. G. & Wittig, N. (2008). Formation of Archaean continental lithosphere and its diamonds: the root of the problem. *Journal of the Geological Society, London* **165**, 895–914.

Pearson, D. G. & Wittig, N. (2014). The formation and evolution of cratonic mantle lithosphere—evidence from mantle xenoliths. In: Holland, H. D. & Turekian, K. K. (eds) *Treatise on Geochemistry Volume 3, 2nd edn*. Elsevier, pp. 255–292.

Pearson, D. G., Canil, D. & Shirey, S. B. (2003). Mantle samples included in volcanic rocks: xenoliths and diamonds. In: Holland, H. D., Turekian, K. K. & Carlson, R. W. (eds) *Treatise on Geochemistry: The Mantle and the Core*. Elsevier, pp. 175–275.

Prelevic, D., Jacob, D. E. & Foley, S. F. (2013). Recycling plus: a new recipe for the formation of Alpine–Himalayan orogenic mantle lithosphere. *Earth and Planetary Science Letters* **362**, 187–197.

Rader, E., Emry, E., Schmerr, N., Frost, D., Cheng, C., Menard, J., Yu, C. Q. & Geist, D. (2015). Characterization and petrological constraints of the midlithospheric discontinuity. *Geochemistry, Geophysics, Geosystems* **16**, 3484–3504.

Rehfeldt, T., Foley, S. F., Jacob, D. E., Carlson, R. W. & Lowry, D. (2008). Contrasting types of metasomatism in dunite, wehrlite and websterite xenoliths from Kimberley, South Africa. *Geochimica et Cosmochimica Acta* **72**, 5722–5756.

Rosing, M. T., Nutman, A. P. & Lofqvist, L. (2001). A new fragment of the early earth crust: the Aasivik terrane of West Greenland. *Precambrian Research* **105**, 115–128.

Salters, V. J. M. & Stracke, A. (2004). Composition of the depleted mantle. *Geochemistry, Geophysics, Geosystems* **5**, Q05B07.

Sand, K. K., Waight, T. E., Pearson, D. G., Nielsen, T. F. D., Makovicky, E. & Hutchison, M. T. (2009). The lithospheric mantle below Southern West Greenland: a geothermobarometric approach to diamond potential and mantle stratigraphy. *Lithos* **112**, 1155–1166.

Santosh, M. (2013). Evolution of continents, cratons and supercontinents: building the habitable Earth. *Current Science* **104**, 871–879.

Seitz, H. M., Altherr, R. & Ludwig, T. (1999). Partitioning of transition elements between orthopyroxene and clinopyroxene in peridotitic and websteritic xenoliths: new empirical geothermometers. *Geochimica et Cosmochimica Acta* **63**, 3967–3982.

Selway, K., Ford, H. & Kelemen, P. (2015). The seismic mid-lithosphere discontinuity. *Earth and Planetary Science Letters* **414**, 45–57.

Shaw, C. S. J., Thibault, Y., Edgar, A. D. & Lloyd, F. E. (1998). Mechanisms of orthopyroxene dissolution in silica-undersaturated melts at 1 atmosphere and implications for the origin of silica-rich glass in mantle xenoliths. *Contributions to Mineralogy and Petrology* **132**, 354–370.

Sleep, N. H. (2009). Stagnant lid convection and carbonate metasomatism of the deep continental lithosphere. *Geochemistry, Geophysics, Geosystems* **10**, Q11010.

Smith, D. (2013). Olivine thermometry and source constraints for mantle fragments in the Navajo Volcanic Field, Colorado Plateau, southwest United States: implications for the mantle wedge. *Geochemistry, Geophysics, Geosystems* **14**, 693–711.

Sobolev, A. V., Hofmann, A. W., Kuzmin, D. V., Yaxley, G. M., Arndt, N. T., Chung, S. L., Danyushevsky, L. V., Elliott, T., Frey, F. A., Garcia, M. O., Gurenko, A. A., Kamenetsky, V. S., Kerr, A. C., Krivolutskaya, N. A., Matvienkov, V. V., Nikogosian, I. K., Rocholl, A., Sigurdsson, I. A., Sushchevskaya, N. M. & Teklay, M. (2007). The amount of recycled crust in sources of mantle-derived melts. *Science* **316**, 412–417.

Sobolev, N. V., Logvinova, A. M., Zedgenizov, D. A., Pokhilenko, N. P., Malygina, E. V., Kuzmin, D. V. & Sobolev, A. V. (2009). Petrogenetic significance of minor elements in olivines from

diamonds and peridotite xenoliths from kimberlites of Yakutia. *Lithos* **112**, 701–713.

Sun, S-s. & McDonough, W. F. (1989). Chemical and isotopic systematics of oceanic basalts: implications for mantle composition and processes. In: Saunders, A. D. & Norry, M. J. (eds) *Magmatism in the Ocean Basins*. Geological Society, London, Special Publications **42**, 313–345.

Tappe, S., Foley, S. F., Stracke, A., Romer, R. L., Kjarsgaard, B. A., Heaman, L. M. & Joyce, N. (2007). Craton reactivation on the Labrador Sea margins: $^{40}Ar/^{39}Ar$ age and Sr–Nd–Hf–Pb isotope constraints from alkaline and carbonatite intrusives. *Earth and Planetary Science Letters* **256**, 433–454.

Tappe, S., Foley, S. F., Kjarsgaard, B. A., Romer, R. L., Heaman, L. M., Stracke, A. & Jenner, G. A. (2008). Between carbonatite and lamproite—Diamondiferous Torngat ultramafic lamprophyres formed by carbonate-fluxed melting of cratonic MARID-type metasomes. *Geochimica et Cosmochimica Acta* **72**, 3258–3286.

Tappe, S., Steenfelt, A., Heaman, L. M. & Simonetti, A. (2009). The newly discovered Jurassic Tikiusaaq carbonatite–aillikite occurrence, West Greenland, and some remarks on carbonatite–kimberlite relationships. *Lithos* **112**, 385–399.

Tappe, S., Pearson, D. G., Nowell, G., Nielsen, T., Milstead, P. & Muehlenbachs, K. (2011a). A fresh isotopic look at Greenland kimberlites: Cratonic mantle lithosphere imprint on deep source signal. *Earth and Planetary Science Letters* **305**, 235–248.

Tappe, S., Smart, K. A., Pearson, D. G., Steenfelt, A. & Simonetti, A. (2011b). Craton formation in Late Archean subduction zones revealed by first Greenland eclogites. *Geology* **39**, 1103–1106.

Tappe, S., Steenfelt, A. & Nielsen, T. (2012). Asthenospheric source of Neoproterozoic and Mesozoic kimberlites from the North Atlantic craton, West Greenland: new high-precision U–Pb and Sr–Nd isotope data on perovskite. *Chemical Geology* **320–321**, 113–127.

Tappe, S., Romer, R. L., Stracke, A., Steenfelt, A., Smart, K. A., Muehlenbachs, K. & Torsvik, T. H. (2017). Sources and mobility of carbonate melts beneath cratons, with implications for deep carbon cycling, metasomatism and rift initiation. *Earth and Planetary Science Letters* **466**, 152–167.

Taylor, W. R. (1998). An experimental test of some geothermometer and geobarometer formulations for upper mantle peridotites with application to the thermobarometry of fertile lherzolite and garnet websterite. *Neues Jahrbuch für Mineralogie, Abhandlungen* **172**, 381–408.

van Acken, D., Luguet, A., Pearson, D. G., Nowell, G. M., Fonseca, R. O. C., Nagel, T. J. & Schulz, T. (2017). Mesoarchean melting and Neoarchean to Paleoproterozoic metasomatism during the formation of the cratonic mantle keel beneath West Greenland. *Geochimica et Cosmochimica Acta* **203**, 37–53.

van Westrenen, W., Blundy, J. & Wood, B. (1999). Crystal-chemical controls on trace element partitioning between garnet and anhydrous silicate melt. *American Mineralogist* **84**, 838–847.

Wang, H. L., van Hunen, J., Pearson, D. G. & Allen, M. B. (2014). Craton stability and longevity: the roles of composition-dependent rheology and buoyancy. *Earth and Planetary Science Letters* **391**, 224–233.

Windley, B. F. & Garde, A. A. (2009). Arc-generated blocks with crustal sections in the North Atlantic craton of West Greenland: crustal growth in the Archean with modern analogues. *Earth-Science Reviews* **93**, 1–30.

Witt-Eickschen, G. & O'Neill, H. S. (2005). The effect of temperature on the equilibrium distribution of trace elements between clinopyroxene, orthopyroxene, olivine and spinel in upper mantle peridotite. *Chemical Geology* **221**, 65–101.

Wittig, N., Pearson, D. G., Webb, M., Ottley, C. J., Irvine, G. J., Kopylova, M., Jensen, S. M. & Nowell, G. M. (2008). Origin of cratonic lithospheric mantle roots: a geochemical study of peridotites from the North Atlantic Craton, West Greenland. *Earth and Planetary Science Letters* **274**, 24–33.

Wittig, N., Webb, M., Pearson, D. G., Dale, C. W., Ottley, C. J., Hutchison, M., Jensen, S. M. & Luguet, A. (2010). Formation of the North Atlantic Craton: timing and mechanisms constrained from Re–Os isotope and PGE data of peridotite xenoliths from SW Greenland. *Chemical Geology* **276**, 166–187.

Woodland, A. B. & Koch, M. (2003). Variation in oxygen fugacity with depth in the upper mantle beneath the Kaapvaal craton, Southern Africa. *Earth and Planetary Science Letters* **214**, 295–310.

Woodland, A. B., Kornprobst, J., McPherson, E., Bodinier, J. L. & Menzies, M. A. (1996). Metasomatic interactions in the lithospheric mantle: petrologic evidence from the Lherz massif, French Pyrenees. *Chemical Geology* **134**, 83–112.

Wyllie, P. J. (1980). The origin of kimberlite. *Journal of Geophysical Research* **85**, 6902–6910.

Yaxley, G. M., Berry, A. J., Kamenetsky, V. S., Woodland, A. B. & Golovin, A. V. (2012). An oxygen fugacity profile through the Siberian Craton—Fe K-edge XANES determinations of $Fe^{3+}/\Sigma Fe$ in garnets in peridotite xenoliths from the Udachnaya East kimberlite. *Lithos* **140**, 142–151.

Yaxley, G. M., Crawford, A. J. & Green, D. H. (1991). Evidence for carbonatite metasomatism in spinel peridotite xenoliths from Western Victoria, Australia. *Earth and Planetary Science Letters* **107**, 305–317.

Yaxley, G. M., Green, D. H. & Kamenetsky, V. (1998). Carbonatite metasomatism in the southeastern Australian lithosphere. *Journal of Petrology* **39**, 1917–1930.

Ziberna, L., Klemme, S. & Nimis, P. (2013). Garnet and spinel in fertile and depleted mantle: insights from thermodynamic modelling. *Contributions to Mineralogy and Petrology* **166**, 411–421.